NIST Technical Note 1958

Numerical Modeling and Analysis of Heat Transfer in Composite Slabs with Profiled Steel Decking

Jian Jiang
Joseph A. Main
Fahim Sadek
Jonathan M. Weigand

This publication is available free of charge from:
https://doi.org/10.6028/NIST.TN.1958

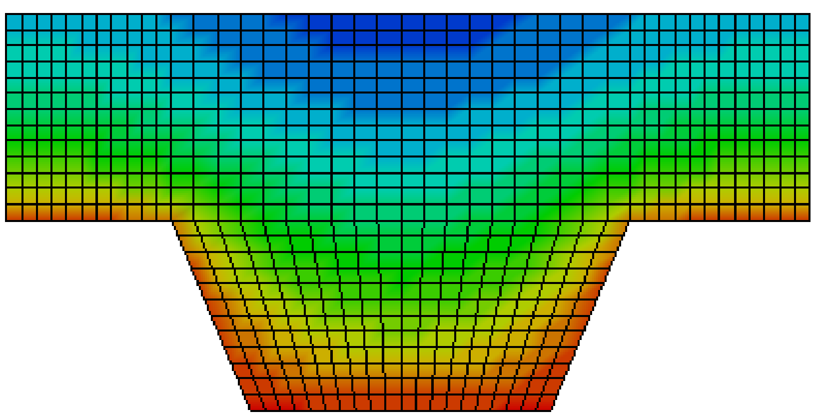

National Institute of Standards and Technology
U.S. Department of Commerce

NIST Technical Note 1958

Numerical Modeling and Analysis of Heat Transfer in Composite Slabs with Profiled Steel Decking

Jian Jiang
Joseph A. Main
Fahim Sadek
Jonathan M. Weigand
Engineering Laboratory
National Institute of Standards and Technology

This publication is available free of charge from:
https://doi.org/10.6028/NIST.TN.1958

April 2017

U.S. Department of Commerce
Wilbur L. Ross, Jr., Secretary

National Institute of Standards and Technology
Kent Rochford, Acting NIST Director and Under Secretary of Commerce for Standards and Technology

National Institute of Standards and Technology Technical Note 1958
Natl. Inst. Stand. Technol. Tech. Note 1958, 68 pages (April 2017)
CODEN: NTNOEF

This publication is available free of charge from:
https://doi.org/10.6028/NIST.TN.1958

ABSTRACT

This report presents detailed and reduced-order finite element modeling of heat transfer in composite floor slabs with profiled steel decking. The detailed modeling approach uses solid elements for the concrete slab and shell elements for the steel decking. The reduced-order modeling approach represents the thick and thin parts of a composite slab with alternating strips of layered shell elements. In the reduced-order modeling approach, a linear gradient in the density of concrete in the rib is used to represent the tapered profile of the rib. In order to more accurately account for the heat input through web of the steel decking in the reduced-order models, the specific heat of concrete in the rib is modified and a dummy material with low specific heat and high thermal conductivity is added in the thin part of the slab. The detailed modeling approach is validated against experimental results available in the literature, and the reduced-order modeling approach is calibrated against the detailed model results and validated against experimental data. A parametric study using the detailed modeling approach is carried out to investigate the influence of the thermal boundary conditions, thermal properties of materials, and slab geometry on the temperature distribution in the composite slab. The results show that the rib height of the decking and the width at the top of the rib are key factors governing the temperature distribution in the rib. In addition, a mesh-sensitivity analysis is performed to investigate the extent to which the element size could be increased while maintaining sufficient accuracy.

Keywords: heat transfer; composite slab; detailed model; reduced-order model.

PREFACE

The numerical study reported herein is part of a comprehensive research program being carried out by the National Institute of Standards and Technology (NIST) on performance-based design methodologies for structures in fire.

TABLE OF CONTENTS

LIST OF FIGURES

LIST OF TABLES

Chapter 1
INTRODUCTION

1.1 BACKGROUND

Typical steel/concrete composite floor slab construction consists of a concrete topping cast on top of profiled steel decking, as illustrated in Figure 1–1. The concrete is typically lightly reinforced with an anti-crack mesh (welded wire mesh) and may also contain individual reinforcing bars, sometimes placed within the ribs. The decking also acts as reinforcement, with indentations in the decking providing mechanical bond with the concrete. Consequently, the composite slab has a low center of reinforcement compared to a conventional flat reinforced concrete slab, thus requiring less concrete. Another advantage of composite slabs over conventional flat slabs is reduced construction time, since the decking serves as permanent formwork. The use of composite slabs in buildings has been common in North America for many years and has experienced a rapid increase in Europe since the 1980s. The presence of the ribs creates an orthotropic profile, which results in thermal and structural responses that are more complex than those for flat slabs, presenting challenges in numerical analysis and practical design for fire effects.

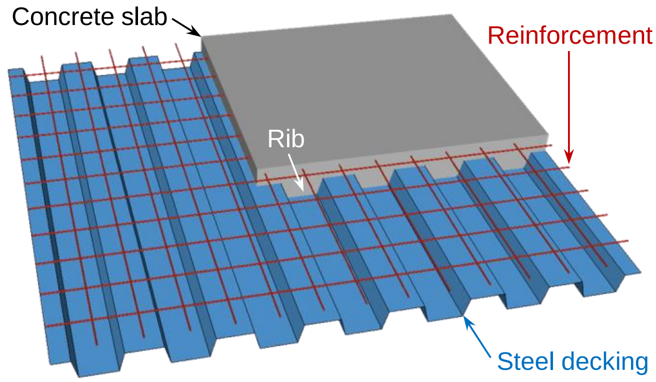

Figure 1–1. Typical layout of a composite slab

Analyzing the response of composite slabs to fire-induced thermal loading requires both heat transfer analyses and structural analyses. The temperatures resulting from heat transfer influence the structural response of the slab through thermal expansion and through degradation of material stiffness and strength. Thermal gradients through the depth of the slab can also produce curvatures, potentially introducing additional bending moments into the floor system. Both thermal and structural analyses of composite slabs present their own unique challenges, and different types of models would typically be used for each analysis. This introduces an additional challenge of transferring analysis results between models with potentially different element types and mesh resolutions. A key objective of this study is to develop a reduced-order modeling approach for thermal analysis that is also suitable for structural analysis. This would allow the same finite element mesh to be used for both types of analyses, facilitating the analysis of structural responses under various fire scenarios, with realistic thermal loading applied from computational fluid dynamic fire simulations. Therefore, while the focus of this study is on thermal analysis, modeling challenges and requirements for subsequent structural analysis must also be considered. The following review summarizes previous research results relevant to both thermal and structural analysis of composite slabs.

Challenges in numerical analysis of heat transfer in composite slabs include appropriate modeling of the thermal boundary conditions on the fire-exposed surfaces and proper modeling of heat transfer at the interface between the concrete slab and the steel decking. Previous studies have generally used a detailed finite-element modeling approach, with solid elements for the concrete slab and shell elements for the steel decking. Researchers from the Netherlands Organization for Applied Scientific Research (TNO) developed a thermo-mechanical model of fire-exposed composite slabs in which an artificial void was introduced to model the radiation heat exchange between the fire environment and the steel decking (Hamerlinck *et al.*, 1990; Both *et al.*, 1992). The artificial void was bounded by an additional artificial surface where the ISO 834 (International Organization for Standardization, 2014) standard fire curve was specified. This method avoided the introduction of empirical view factors (see Section 2.1). Lamont *et al.* (2004) and Guo (2012) introduced interface elements to model heat transfer between the steel deck and the concrete slab in finite element thermal analyses of composite slabs. Pantousa *et al.* (2013) simplified the modeling of this interface in thermo-mechanical analysis of composite slabs by sharing nodes between the shell elements representing the steel decking, and the solid elements representing the adjacent concrete, by assuming continuity of temperature at their interface.

Challenges in structural analysis of composite slabs include properly accounting for the orthotropic behavior associated with the profiled decking, as well as capturing the effects of material and geometric nonlinearities expected during the response. While a few studies have used detailed models with solid elements to analyze the structural response of composite slabs in analyses of column loss at ambient room temperatures (e.g., Sadek *et al.*, 2008; and Alashker *et al.*, 2010), reduced-order modeling approaches are generally preferable for simulating large-scale composite frames. Although a considerable amount of research has focused on reduced-order modeling of conventional reinforced concrete slabs, reduced-order modeling of ribbed composite slabs with profiled steel decking has received less attention. One approach employed a grillage of beam elements to approximate the bending and membrane response of a composite slab (Elghazouli *et al.*, 2000; Elghazouli and Izzuddin, 2000; Sanad *et al.*, 2000). The composite slab was modeled as a grillage of T-section beams along the rib direction and flat rectangular beams in the transverse direction, and the results showed that the influence of the ribs across the bottom of the slabs was significant and should be accounted for. The disadvantage of the grillage-type modeling lies in its inability to properly simulate the development of membrane action, in which loads are resisted by tensile forces in the reinforcement, in conjunction with compressive forces in the concrete along the edges of slabs. Huang *et al.* (2000) and Izzuddin *et al.* (2004) developed modified shell element formulations that allowed shell elements of uniform thickness to represent the orthotropic behavior of a composite slab. Specifically, Huang *et al.* (2000) applied an effective stiffness factor to modify the material stiffness matrices of plain concrete to account for the orthotropic properties of the slab, while Izzuddin *et al.* (2004) introduced a flat shell element for ribbed composite slabs that accounted for geometric and material nonlinearities and incorporated two additional displacement fields corresponding to stretching and shear modes in the rib, thus accounting for the effect of the rib on the membrane and bending actions transverse to the rib orientation. To represent the orthotropic properties of a composite slab, Lim *et al.* (2004) proposed an approach in which shell elements were used to represent the continuous concrete slab above the decking and beam elements were used to represent the ribs. Using a similar approach, Yu *et al.* (2008) developed an orthotropic slab element assembled from a layered plate element representing the continuous concrete slab and a beam element representing a group of ribs. Finally, Kwasniewski (2010) and Main (2015) proposed approaches in which alternating strips of layered shell elements were used to represent the thick and thin parts of a composite slab, and verification of these modeling approaches under column loss scenarios was presented through comparisons with detailed finite element analyses in which the slab was represented with solid elements and the steel decking with shell elements.

In previous structural analyses of composite slabs under fire loading (e.g., Lamont *et al.*, 2004; Lim *et al.*, 2004; Foster *et al.*, 2007; and Yu *et al.*, 2008), temperature histories were prescribed within the structural analysis model, and the suitability of the modeling approach for thermal analysis was not considered. In considering the suitability of the various reduced-order modeling approaches previously used for structural analysis for heat transfer analysis, the grillage approach with beam elements has significant limitations, because of the inadequacy of the 1-dimensional (1D) elements to represent in-plane and through-thickness heat transfer in the slab. Modeling approaches that use the same shell thicknesses for the thick and thin parts of the slab also have limitations for thermal analysis, because they fail to capture the shielding effect of the ribs, which results in curved isotherms in the floor slab. This significantly affects both the structural response and the thermal insulation provided by the slab. Because of the inadequacy of 1D elements to capture the complexities of heat transfer in composite floor slabs, hybrid approaches that use both shell and beam elements are also limiting. The modeling approach that uses alternating strips of shell elements, however, has the potential to capture both in-plane and through-thickness heat transfer in composite slabs, including the shielding effect of the ribs. As a result, this approach is adopted in this study.

1.2 SCOPE OF STUDY

A key objective of this study is to develop a reduced-order modeling approach for heat transfer analysis of composite slabs that is also suitable for structural analysis, so that the same model can be used for both thermal and structural analysis. To achieve this objective, detailed and reduced-order finite element modeling approaches were developed for heat transfer analysis in composite floor slabs with profiled steel decking. Factors influencing heat transfer in composite slabs are reviewed in Chapter 2. The detailed modeling approach, described in Chapter 3, used solid elements for the concrete slab and shell elements for the steel decking. After validation of the detailed modeling approach against experimental data available in the literature, detailed models of composite slabs were used to conduct a parametric study by varying the thermal boundary conditions, thermal properties of the materials, and slab geometry, as described in Chapter 4. A mesh sensitivity analysis was also performed to investigate the extent to which the element size in the detailed modeling approach could be increased while still maintaining sufficient accuracy. Based on understanding the temperature distribution in composite slabs from the detailed models, a reduced-order modeling approach consisting of alternating strips of layered shell elements for the thick and thin parts of the slab was proposed, as described in chapter 5. A linear gradient in the density of concrete in the rib was used to represent the tapered profile of the rib. Since the layered shell formulation cannot directly consider heat input through the web of the decking, this effect was accounted for by (1) introducing a “dummy material” with high through-thickness thermal conductivity and negligible specific heat to represent the absence of material between the ribs of the slab and (2) modifying the specific heat of concrete in the ribs to achieve better agreement with temperature histories obtained from detailed models. The reduced-order modeling approach was calibrated and verified against the detailed models for a wide range of slab geometries, and was also validated against available experimental results. Chapter 6 summarizes the results of this study and presents the main conclusions.

This page intentionally left blank.

Chapter 2
HEAT TRANSFER IN COMPOSITE SLABS

This chapter presents a review of key factors influencing heat transfer in composite slabs. General considerations applicable to both the detailed modeling approach (Chapter 3) and the reduced-order modeling approach (Chapter 5) are discussed, and properties used in the subsequent analyses are presented.

2.1 HEAT EQUATION AND BOUNDARY CONDITIONS

Heat can be transferred by three methods: conduction, convection, and radiation. Conduction is the transfer and distribution of heat energy from atom to atom within a substance. Convection is the transfer of heat by the movement of medium (i.e., advection and/or diffusion of a gas or liquid). Radiation is the transfer of heat via electromagnetic waves.

The heat conduction balance in a solid structural member under fire conditions is given by the heat equation (e.g., Lienhard, 2011):

$$\lambda_x \frac{\partial^2 T}{\partial x^2} + \lambda_y \frac{\partial^2 T}{\partial y^2} + \lambda_z \frac{\partial^2 T}{\partial z^2} = \rho c \frac{\partial T}{\partial t} \ , \tag{2.1}$$

where λ_x, λ_y, and λ_z are the thermal conductivities of the material in the x, y, z, directions, respectively; T is the temperature; t is time; ρ is the density of the material; and c is the specific heat of the material.

To solve Eq. (2.1), heat transfer boundary conditions (i.e., convection and radiation heat fluxes) should be provided on the surface between the structural member or fireproofing and gas environment. The boundary conditions can be written as:

$$-\lambda_n \frac{\partial T}{\partial n} = \dot{q}_c'' + \dot{q}_r'' = h_c (T_s - T_g) + \sigma \varepsilon_r \Phi (T_s^4 - T_g^4) \ , \tag{2.2}$$

where n is a coordinate in the direction of the surface normal; $\dot{q}_c''$ is the heat flux per area from convection, W/m^2; $\dot{q}_r''$ is the heat flux per area from radiation, W/m^2; T_g is the temperature of the gas adjacent to the surface, K; T_s is the surface temperature, K; h_c is the convective heat transfer coefficient, W/(m^2·K); ε_r is the resultant emissivity, defined as $\varepsilon_r = \varepsilon_f \times \varepsilon_s$, where ε_f is the emissivity of fire, usually taken as equal to 1.0, and ε_s is the emissivity of the surface material; $\sigma = 5.67\times10^{-8}$ W/(m^2·K^4) is the Stefan-Boltzmann constant; and Φ is the view factor or configuration factor, which is explained in the next section.

2.2 VIEW FACTOR

The view factor Φ in Eq. (2.2) quantifies the geometric relationship between the surface emitting radiation and the surface receiving radiation. It depends on the areas and orientations of the surfaces, as well as the gap between them. For composite slabs, the view factor of the lower flange of steel decking is generally taken as unity, $\Phi_{low} = 1.0$. The view factors for the web and upper flange of steel decking are less than unity due to obstruction from the ribs. The latter can be calculated following the Hottel's crossed-string method (Nag, 2008), as illustrated in Figure 2–1, which is also the approach adopted by Eurocode 4 (CEN, 2005), hereafter referred to as EC4. Resulting expressions for the view factors of the upper flange and the web of the steel decking, denoted Φ_{up} and Φ_{web}, respectively, are presented in Eqs. (2.3a) and (2.3b), where the geometric parameters h_1, h_2, l_1, l_2, and l_3 are illustrated in Figure 2–2. The parameter l_1 is the total width at the top of the rib, and l_2 and l_3 are the lower-flange and upper-flange widths of the steel decking, respectively.

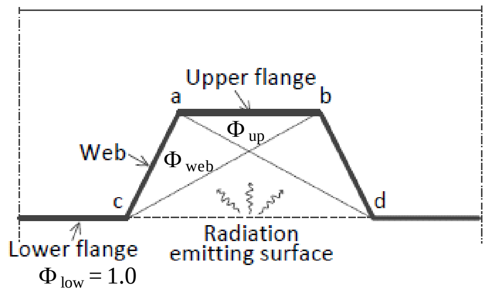

Figure 2–1. Schematic for the calculation of view factor

$$\Phi_{up} = \frac{ad + cb - ab - cd}{2ab} = \frac{\sqrt{h_2^2 + \left(l_3 + \frac{l_1 - l_2}{2}\right)^2} - \sqrt{h_2^2 + \left(\frac{l_1 - l_2}{2}\right)^2}}{l_3} \tag{2.3a}$$

$$\Phi_{web} = \frac{ac + cd - ad}{2ac} = \frac{\sqrt{h_2^2 + \left(\frac{l_1 - l_2}{2}\right)^2} + \left(l_3 + l_1 - l_2\right) - \sqrt{h_2^2 + \left(l_3 + \frac{l_1 - l_2}{2}\right)^2}}{2\sqrt{h_2^2 + \left(\frac{l_1 - l_2}{2}\right)^2}} \tag{2.3b}$$

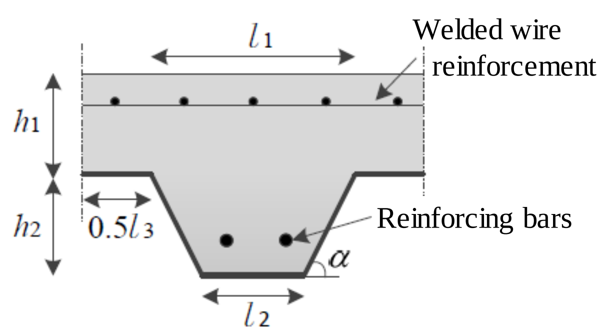

Figure 2–2. Parameters representing the slab geometry

2.3 EMISSIVITY OF GALVANIZED STEEL DECKING

The steel decking of composite slabs is usually made from galvanized cold-formed steel with a thin zinc layer on both faces for protection against corrosion. During heating, the zinc layer melts and deteriorates, leading to a delay in the temperature increase of the decking. This effect can be considered by using a temperature-dependent emissivity of steel. Hamerlinck *et al.* (1990) proposed a model in which the emissivity is assumed to be 0.1 for temperatures below 400 °C, and the emissivity is taken as 0.4 for temperatures in excess of 800 °C, with a linear variation in emissivity between these temperatures. This model by Hamerlinck *et al.* (1990) was the basis for developing the fire resistance tables in Annex D of EC4. However, a constant emissivity of 0.7 is conservatively specified in EC4 for heat transfer calculations for both concrete and steel. Experiments by Both (1998) showed that both the steel temperature and the heating rate influenced the variation of the emissivity. In Section 3.2.1, an alternative temperature-dependent model for the emissivity of galvanized decking is proposed that is somewhat more conservative than the model of Hamerlinck *et al*. (1990) and is found to give improved agreement with experimental data.

2.4 THERMAL MATERIAL PROPERTIES

Thermal properties required for heat transfer analysis include the density, thermal conductivity, and specific heat. For concrete, these properties vary with moisture content and aggregate type. The NIST *Best Practice Guidelines for Structural Fire Resistance Design of Concrete and Steel Buildings* (Phan et al. 2010) present a review of experimental data and practical design recommendations for thermal properties of concrete at elevated temperature. Temperature-dependent values given in EC4 (CEN, 2005) and in the ASCE manual on structural fire protection (ASCE, 1992) are shown in Figure 2–3 and Figure 2–4 for specific heat and thermal conductivity, respectively. Kodur (2014) presented a comprehensive comparison of these properties. Generally, the ASCE manual distinguishes between siliceous and carbonate aggregates, while EC4 applies to all aggregate types. For the analyses in this study, temperature-dependent thermal material properties from EC4 are used for both concrete and steel, unless otherwise specified.

Figure 2–3 shows the specific heat of concrete as a function of temperature for (a) normal-weight concrete and (b) lightweight concrete. The EC4 models for normal-weight and lightweight concrete depend on the moisture content (m.c.). As shown in Figure 2–3, the specific heat ranges between approximately 900 J/(kg·K) and 1200 J/(kg·K) for normal-weight concrete and between approximately 840 J/(kg·K) and 1000 J/(kg·K) for lightweight concrete, with increased values over certain temperature ranges that are associated with phase changes in the moisture or the aggregate. In EC4, the specific heat is increased for temperatures between 100 °C and 200 °C due to the influence of moisture evaporation in the early stage of heating. In the ASCE manual, the specific heat is increased for temperatures between 400 °C and 800 °C due to the phase change of the aggregate, and between 100 °C and 200 °C in EC4 (due to the influence of moisture evaporation in the early stage of heating). Data presented in the NIST *Best Practice Guidelines* (Phan et al. 2010) show increased values of specific heat over a temperature range between 400 °C and 600 °C, associated with phase change of the aggregate. Constant values of 1000 J/(kg·K) and 1170 J/(kg·K) are recommended for simple calculations in EC4 and in the ASCE manual, respectively.

The heat transfer in the slab is significantly influenced by the moisture content of the concrete. During heating, migration and evaporation of moisture occurs, absorbing energy and thus delaying the temperature rise in concrete. The effect of the evaporation of free moisture in concrete is often modeled by modifying the specific heat within a certain temperature range, and the moisture migration is usually ignored. It is often assumed that the free moisture evaporates within a temperature range of 100 °C to 200 °C. A peak specific heat is assumed at, e.g., 115 °C in EC4 (Figure 2–3) for both normal-weight and lightweight concrete. This peak value can be determined from the heat of evaporation of water and the moisture content.

This assumption for moisture content is normally appropriate in fire engineering calculations. The EC4 provides peak values of specific heat for moisture content up to 10 %.

Figure 2–4 shows the variation of the thermal conductivity with temperature for concrete based on data from EC4 and the ASCE manual, as well as experimental results from Kodur (2014). Note that the test results for thermal conductivity are typically higher than the upper limit in EC4 for all temperatures. Figure 2–4 shows that the thermal conductivity depends on the aggregate type. In addition to the dependence on aggregate type, data presented by Phan et al. (2010) show that the moisture content can affect the conductivity of concrete for temperatures below 100 °C, prior to evaporation of moisture.

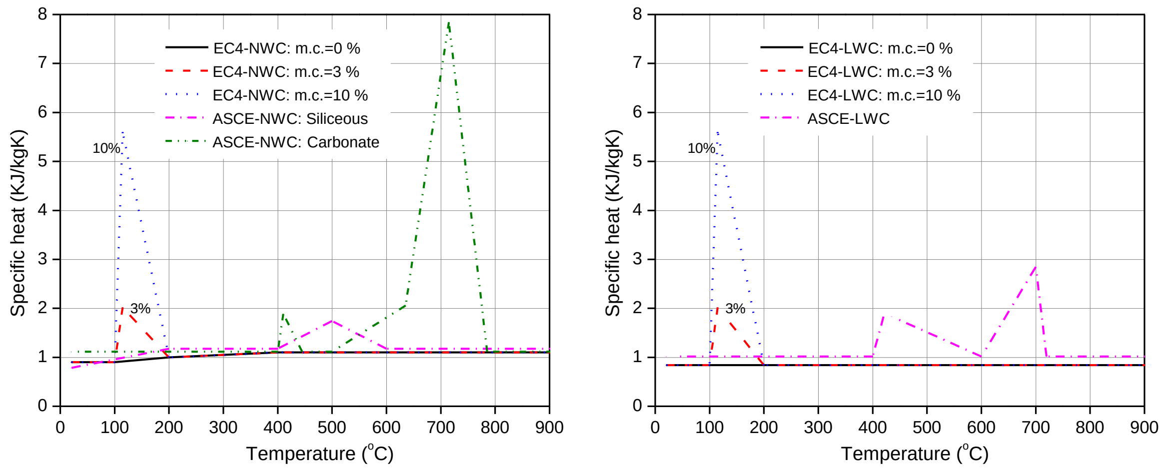

(a) (b)

Figure 2–3. Specific heat of concrete in EC4 (CEN 2005) and ASCE (ASCE 1992): (a) normal-weight concrete (NWC); (b) lightweight concrete (LWC)

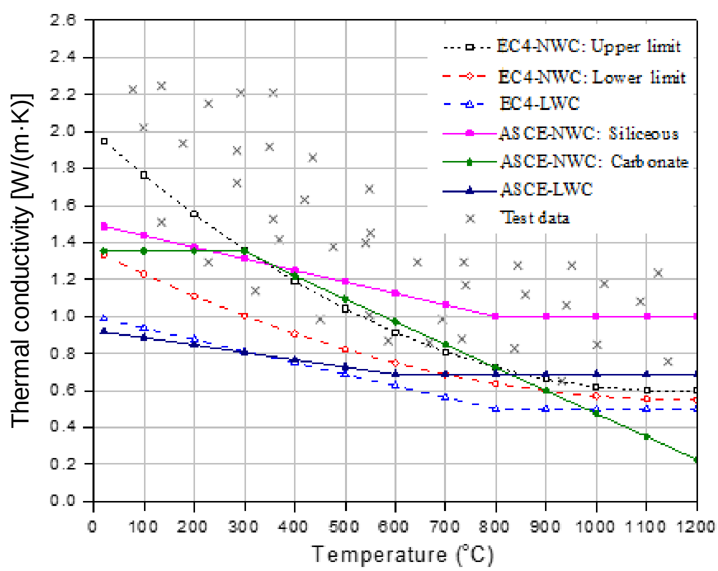

Figure 2–4. Thermal conductivity of concrete in EC4 (CEN 2005) and ASCE (ASCE 1992) along with test data from Kodur (2014)

Chapter 3
DETAILED MODELING APPROACH

This chapter describes the development and validation of a detailed finite-element modeling approach for heat transfer in composite slabs. The detailed modeling approach, as described in Section 3.1, uses solid elements for the concrete slab and shell elements for the steel decking. The detailed modeling approach was validated against two fire tests on composite slabs reported in the literature, as described in Section 3.2. Section 3.3 presents typical temperature distributions in the composite slab, illustrating the curved isotherms that result from non-uniform heat transfer through the profiled composite slab. Finally, as described in Section 3.4, a mesh-sensitivity analysis was also performed to investigate the extent to which the mesh size in the detailed modeling approach could be increased, while maintaining sufficient accuracy in the results.

3.1 DETAILED FINITE-ELEMENT MODELING

In the detailed finite-element modeling approach, the concrete slab was modeled with solid elements and the steel decking was modeled with shell elements. The concrete slab and steel decking had a consistent mesh at their interface and shared common nodes. Noting the periodicity of the composite slab profile and the thermal loading, with the gas temperature T_g assumed to be uniform, only one half-strip of the composite slab was modeled, as shown in Figure 3–1. Adiabatic boundary conditions were assigned at the right and left boundaries of the model to represent the symmetry at these sections in the periodic slab profile. Convection and radiation boundary conditions (Eq. (2.2)) were defined at the top surface of the slab and the bottom surface of the steel decking (i.e., the lower flange, web, and upper flange of the decking labeled in Figure 3–1). Although three-dimensional analyses were performed, with multiple rows of solid and shell elements in the longitudinal direction (i.e., in the direction of the ribs), only two-dimensional heat transfer problems were considered in this study, with the thermal loading and the resulting temperatures being uniform in the longitudinal direction. The heat transfer analyses were performed using the LS-DYNA finite-element software (LSTC, 2014). Steel reinforcement was not explicitly included in the numerical models, but reinforcement temperatures, when needed, can be estimated from the temperature of the concrete at the reinforcement location. Both the concrete and the steel decking were modeled using LS-DYNA thermal material model MAT_T10 (MAT_THERMAL_ISOTROPIC_TD_LC), with the specific heat and thermal conductivity for each material defined as functions of temperature using equations from Eurocode 4 (CEN, 2005), as discussed previously in Section 2.4.

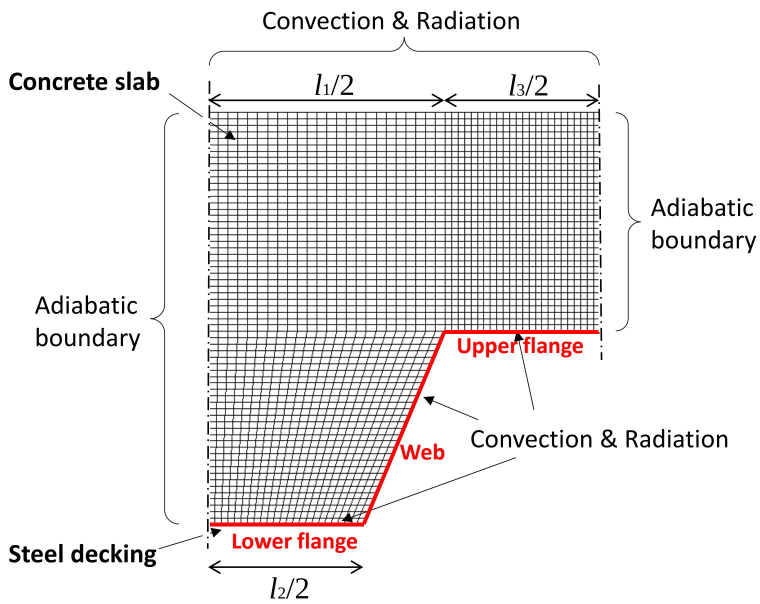

Figure 3–1. Schematic of the detailed model of composite slabs

3.2 VALIDATION OF DETAILED MODELING APPROACH

As described in the following subsections, the detailed modeling approach was validated by comparing the model results with experimental measurements from two different studies. A typical element length of 5 mm was used in the validation analyses, which was found to be adequate based on a mesh sensitivity study reported in Section 3.4.

3.2.1 TNO Test

A standard fire test per ISO 834 (International Organization for Standardization, 2014) on a simply supported one-way concrete slab (Test 2 from Hamerlinck *et al.*, 1990) was selected to validate the proposed detailed modeling approach. Figure 3–2 shows the configuration of the tested slab. The slab had six ribs and used Prins PSV73 steel decking and normal-weight concrete with a measured moisture content of 3.4 %. Heat transfer parameters reported by Hamerlinck *et al.* (1990) were used in the modeling, as summarized in the following. The convective heat transfer coefficient for the lower flange of the steel decking was taken as 25 W/(m^2·K), and a lower value of 15 W/(m^2·K) was used for the web and upper flange of the decking to consider the shielding effect of ribs. A convective heat transfer coefficient of 8 W/(m^2·K) and an emissivity of 0.78 were used for the unexposed top concrete surface. View factors for the upper flange and the web of the steel decking were 0.3 and 0.6, respectively, calculated based on Equation (2.3) (see Section 2.1), and a view factor of 1.0 was used for the lower flange of the steel decking and the unexposed top concrete surface. For the emissivity of the galvanized steel decking, in addition to the temperature-dependent model of Hamerlinck *et al.* (1990) (see Section 2.3), two alternative models were considered: the constant value of 0.7 used in EC4 (CEN, 2005) and a new model proposed in this study, which is described subsequently.

Numerical and experimental temperature histories are compared in Figure 3–3 for several locations in the slab (letters A through K are temperature measurement points shown in Figure 3–2). The numerical results in Figure 3–3 used the model of Hamerlinck et al. 1990) for the emissivity of the decking. The largest percent deviation between the measured and computed temperatures at the end of the test was 10 % (at point A). The percent deviation at the end of the test is used throughout this report to quantify discrepancies between computed and measured temperatures for two reasons. Firstly, deviations are of greatest concern for the maximum temperatures in the latter stages of heating, which are the most critical in design. Secondly, percent deviations are not very meaningful in the early stages of heating when the temperatures (in °C) have small numerical values. For the results in Figure 3–3, the agreement between the computed and measured temperatures was generally better in the upper continuous part of the slab (points E through K) than in the rib (points A through C).

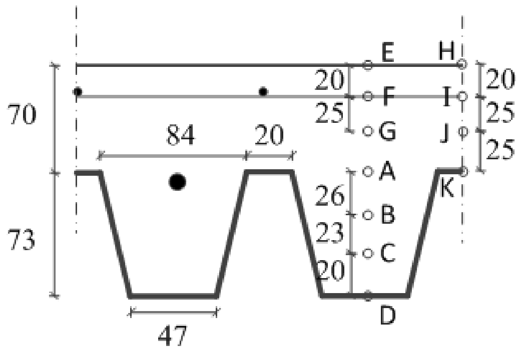

Figure 3–2. Geometry of TNO tested slab (Hamerlinck *et al.*, 1990) (dimensions in mm)

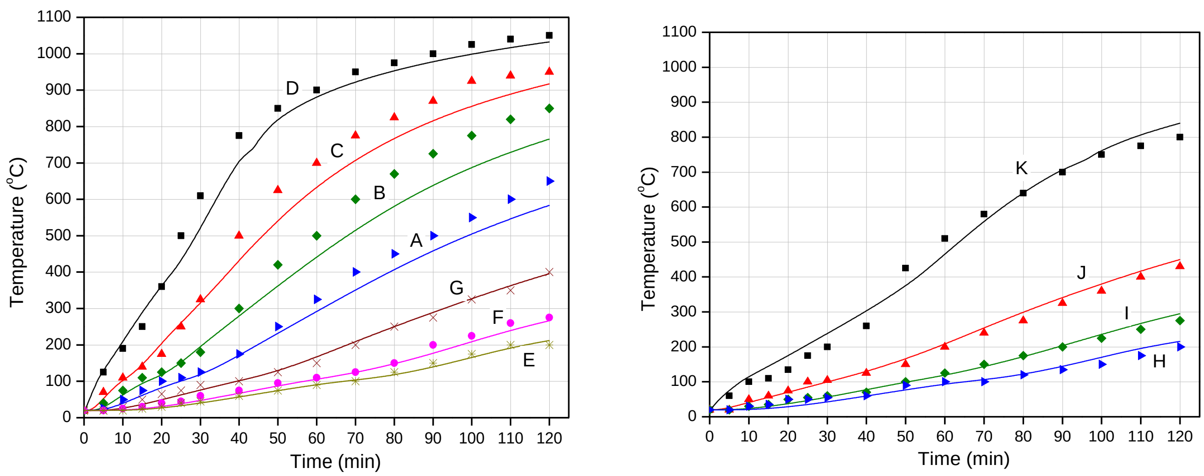

(a) (b)

Figure 3–3. Comparison of calculated (solid curves) and measured (discrete symbols) temperatures at: (a) the thick part; (b) the thin part

The difference between the numerical and test results in Figure 3–3 (especially at Points A, B, and C) was likely due to the influence of the change in emissivity of the galvanized steel decking as a result of melting of the zinc layer, since the predicted temperatures were somewhat lower than the measured results, and since the difference was more pronounced after 30 min of heating, when the temperature of the decking exceeded 400 °C. The EC4 (CEN, 2005) conservatively recommends a temperature-independent emissivity value of 0.7 for steel. Figure 3–4 shows a comparison of the temperature histories at Points A, B, and C between the test results, the detailed model results based on the constant EC4 emissivity, and the detailed model results based on the temperature-dependent emissivity from Hamerlinck *et al.* (1990). It shows that the predicted temperatures based on the Hamerlinck *et al.* model were closer to the test results in the early stage of heating (up to 30 min), while the EC4 predictions were closer to the test results in the later stages of heating (after 80 min). This indicates that the larger emissivity of 0.7 may be more appropriate than 0.4 for temperatures exceeding 800 °C. In this study, a new model for the temperature-dependent emissivity of steel is proposed as follows:

$$\varepsilon_s = \begin{cases} 0.1 & T \leq 400\ ℃ \\ 0.1 + 0.0015 \cdot (T - 400\ ℃) & 400\ ℃ < T < 800\ ℃ \\ 0.7 & T \geq 800\ ℃ \end{cases}, \tag{3.1}$$

where at temperatures below 400 °C and above 800 °C, emissivities of 0.1 and 0.7, respectively, are assumed, with a linear variation between 0.1 and 0.7 for temperatures between 400 °C and 800 °C. Figure 3–5 shows a comparison of the temperature histories at Points A, B, and C between the test results, the detailed model results based on emissivity from Hamerlinck *et al.* (1990), and the detailed model results based on the emissivity model proposed in this study. This figure shows that the increased emissivity at larger temperatures yields higher temperatures by up to 70 °C (Point B at time 90 mins) when compared with the temperature histories using the emissivity from Hamerlinck *et al.* (1990). Better agreement with the experimental results was observed using the proposed model. Figure 3–6 shows a comparison of temperature histories in the slab between test results and detailed model with the proposed emissivity of steel in Eq. (3.1). The differences between the measured and computed temperatures at the end of the test in this case did not exceed 5 %. The temperature contours in the slab for the two emissivity models after two hours of heating are shown in Figure 3–7. The proposed emissivity of steel resulted in high temperatures in a larger area of concrete in the rib.

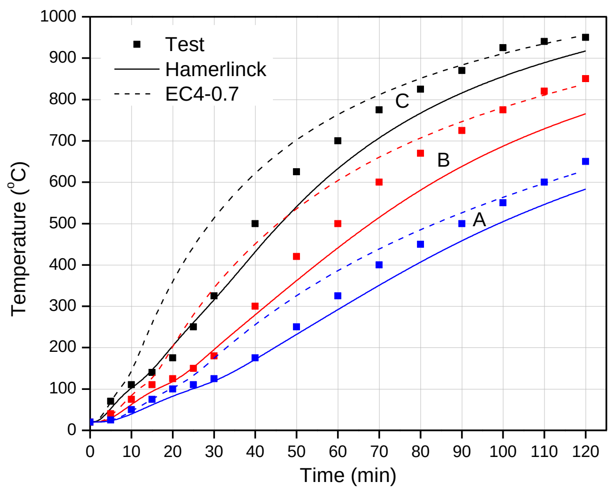

Figure 3–4. Comparison of temperature in the rib between test, EC4 and Hamerlinck model

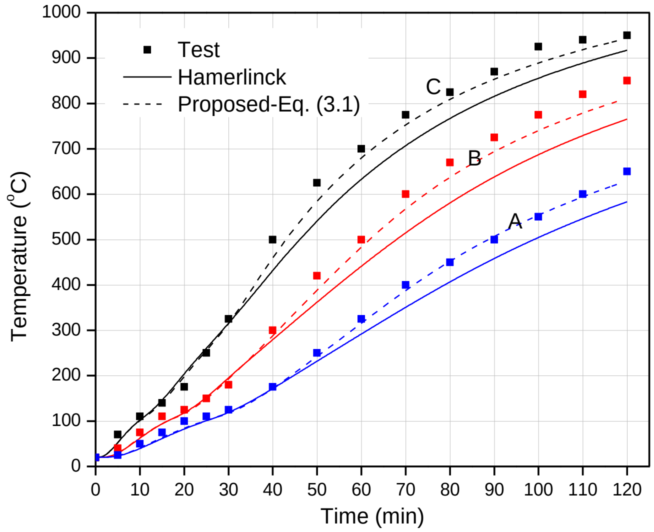

Figure 3–5. Comparison of temperature in the rib between test results and numerical model based on emissivity from Hamerlinck *et al.* (1990) and from proposed model

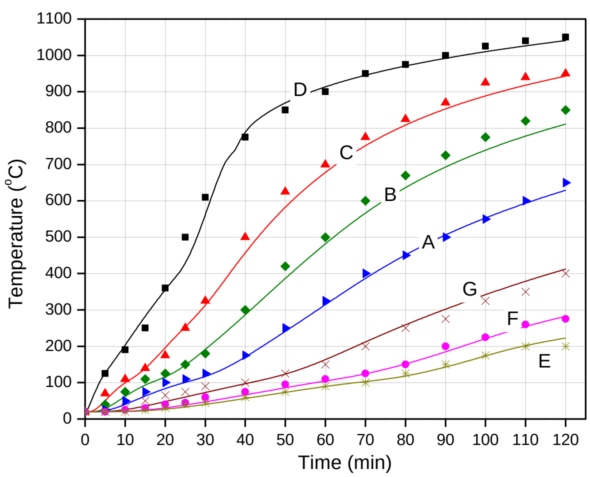

(a)

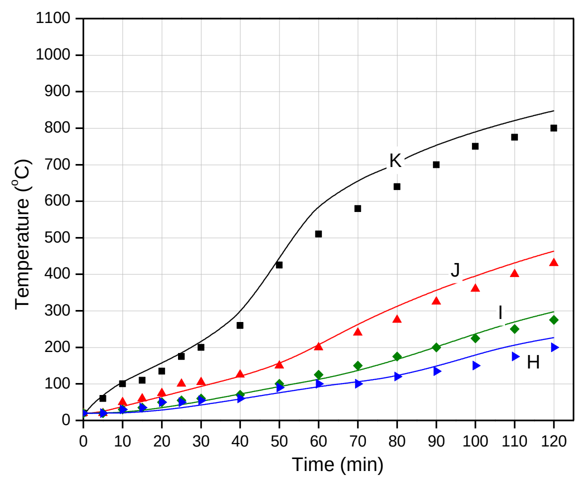

(b)

Figure 3–6. Comparison of measured (discrete symbols) and calculated (solid curves) temperatures using proposed emissivity of decking in Eq. (3.1) at: (a) the thick part; (b) the thin part

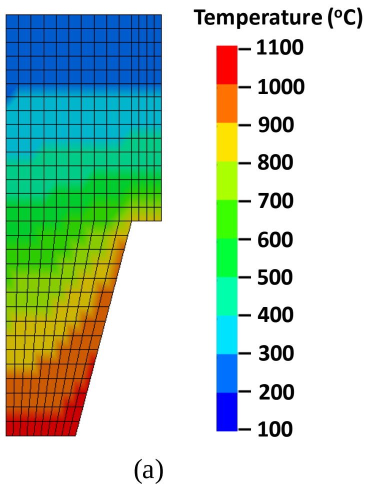

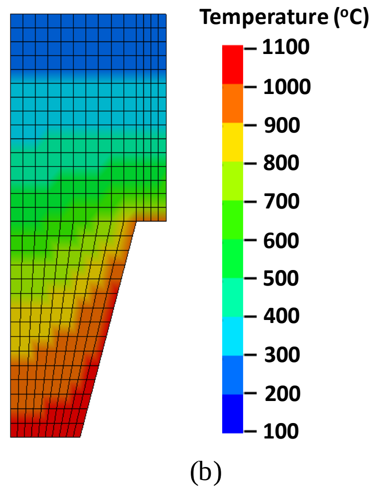

Figure 3–7. Temperature contours in the tested slab (at 120 min): (a) emissivity from Hamerlinck *et al.* (1990); (b) proposed emissivity in Eq. (3.1)

3.2.2 BRANZ Test

The detailed modeling approach was also validated against a two-way composite slab tested in the Building Research Association of New Zealand (BRANZ) furnace (Lim, 2003). The configuration of the slab's cross section is shown in Figure 3–8. The tested slab was 3.15 m wide and 4.15 m long, and was exposed to the ISO 834 fire for 3 hours. The Dimond Hibond steel decking had a thickness of 0.75 mm and a total depth of 130 mm. Normal-weight concrete was used with siliceous aggregates. In the detailed model of the slab, the same thermal loading and boundary conditions as the TNO test were used. Heat transfer analyses were conducted using steel emissivity from Hamerlinck *et al.* (1990) and from the model proposed in this study (Eq. 3.1). Comparison of numerical and experimental results is presented in Figure 3–9 for Points A through E (shown in Figure 3–8).

Figure 3–9 shows only small differences between the temperatures predicted by the two emissivity models. The largest percent deviation between the experimental and computational results at the end of the test was 12 % for the emissivity model of Hamerlinck *et al.* (1990) and 10 % for the proposed emissivity model, both at point D. The largest-magnitude deviation between the test and model results was observed at point A, which was located at the bottom surface of the concrete slab, where maximum temperature deviations of 135 °C and 192 °C were observed for the model of Hamerlinck *et al.* (1990) and for the proposed emissivity model, respectively, with corresponding percent deviations of 9 % and 10 % at the end of the test. The large temperature differences at point A were due to debonding of the steel decking from the concrete slab that was observed in the test (Lim, 2003), which disrupted the heat transfer from the steel decking to the lowermost surface of the concrete slab in the experiment, leading to lower measured temperatures. Numerical results provided by Lim (2003) are also included in Figure 3–10 for comparison. Temperature contours at 180 min from the numerical simulation with the two different emissivity models are shown in Figure 3–11, in which slightly higher temperatures are evident for the proposed emissivity model. The following section provides further discussion of the temperature distribution in a typical composite slab under fire exposure.

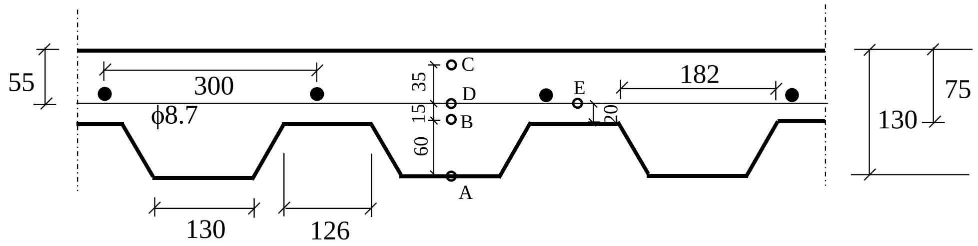

Figure 3–8. Geometry of BRANZ tested slab (Lim 2003) (dimensions in mm)

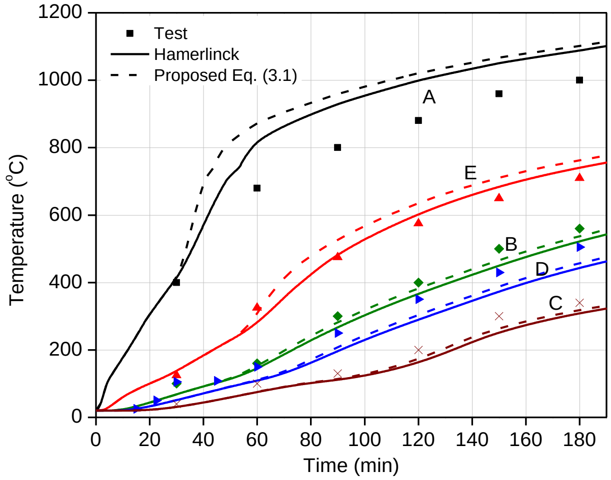

Figure 3–9. Comparison of measured (discrete symbols) and calculated (solid curves) temperatures

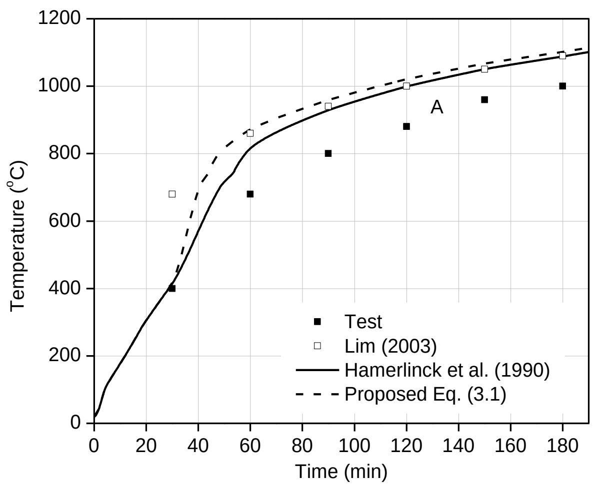

Figure 3–10. Comparison of the temperature at Point A

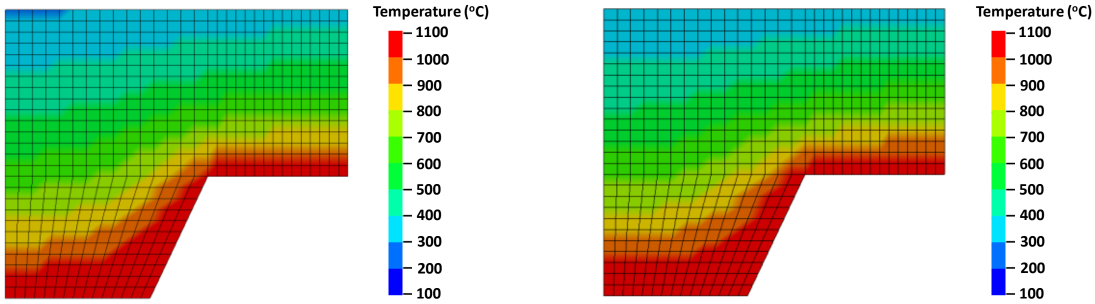

(a) (b)

Figure 3–11. Temperature contours in the BRANZ tested slab (at 180 min): (a) emissivity from Hamerlinck *et al.* (1990); (b) proposed emissivity in Eq. (3.1)

3.3 TEMPERATURE DISTRIBUTION IN TYPICAL COMPOSITE SLAB

Figure 3–12 illustrates a typical composite slab configuration used in North America, with an 85 mm concrete topping on 75 mm steel decking. The geometry of the decking in Figure 3–12 corresponds to Vulcraft 3VLI decking. The typical slab configuration illustrated in Figure 3–12 is used for the mesh-sensitivity study in the following section, as the baseline case for the parametric study in Chapter 4, and as the baseline case for the development of the reduced-order modeling approach in Chapter 5.

A temperature distribution in one half-strip of the typical composite slab is shown in Figure 3–13. The temperature contours in the slab exhibit curved isotherms that generally follow the profile of the steel decking, with reduced curvature of the isotherms near the top of the slab. During fire exposure, heat is input from the fire to the bottom of the slab by means of convection and radiation. Fireproofing is not typically applied to the steel decking, and therefore the temperature of the decking rises quickly (Points A and F in Figure 3–13a). The web and upper flange of the decking have a slightly lower temperature than the lower flange due to the shielding effect of the rib (compare the temperature histories for points A and F in Figure 3–13b). Because of the large heat capacity of the concrete slab, the temperature of the steel decking is significantly lower than the gas temperature in the early stages of heating but converges to the gas temperature in the later stages (compare temperature histories for points A and F with the gas temperature in Figure 3–13b). As Figure 3–13 indicates, the temperature increase within the concrete slab is slow, relative to that of the steel decking. Higher temperatures are evident in the thin part of the slab (Points F, G, and H) than in the thick part (Points A, B, D, and E), resulting in a non-uniform temperature distribution along any horizontal plane in the upper continuous portion of the slab. The maximum temperature at the unexposed side of the slab (Point H) determines the thermal insulation provided by the composite slab.

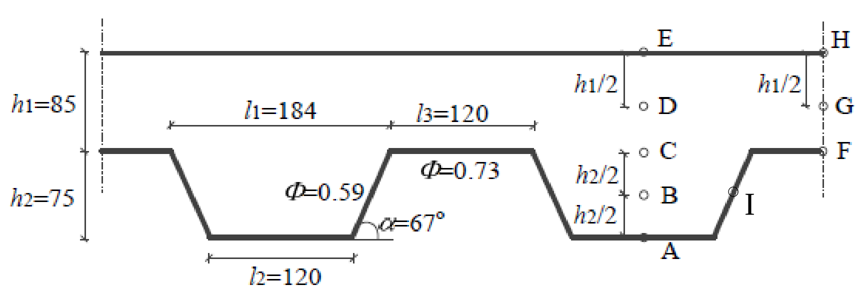

Figure 3–12. Typical composite slab configuration with Vulcraft 3VLI decking (dimensions in mm)

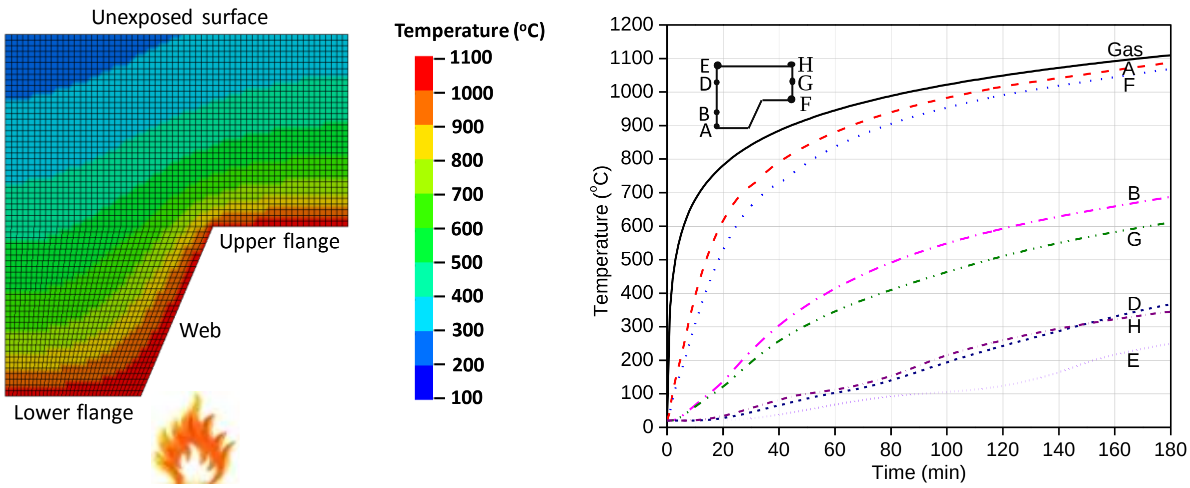

(a) (b)

Figure 3–13. Temperature distribution in a typical composite slab: (a) temperature contours after three hours of heating; (b) temperature histories at selected locations

3.4 MESH SENSITIVITY OF DETAILED MODEL

In this study, a fine mesh is always used in the detailed modeling approach (see, e.g., Figure 3–1). However, for structural analysis of large-scale composite floor systems (see, e.g., Sadek *et al.*, 2008), a relatively coarse mesh is preferable in order to reduce the computational burden. In this section, a sensitivity analysis is performed to study the effect of mesh refinement on the computed temperature distribution within composite slabs. Three alternative coarse meshes were considered, as shown in Figure 3–14, which are designated as the 2×2, 4×4, and 8×8 meshes. In the mesh designation $n \times n$, n is the number of elements across the width of the rib, which is the same as the number of elements through the depth of the rib. A consistent mesh was used for the upper continuous portion of the slab.

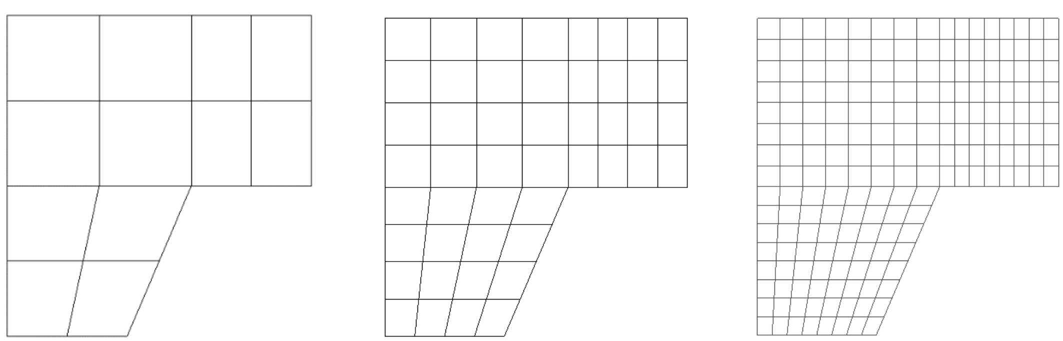

(a) (b) (c)

Figure 3–14. Alternative coarse meshes for composite slabs: (a) 2×2; (b) 4×4; (c) 8×8

The same analysis conducted using a fine mesh in Section 3.3 was repeated using the three coarse meshes, and Figure 3–15 shows a comparison of the resulting temperature histories at various points in the slab. Compared with the fine mesh (average element length of 2.5 mm), the 2×2 coarse mesh (average element length of 30 mm) yielded lower temperatures in the steel decking (points A, I, and F) and higher temperatures at the unexposed top surface of the slab (points E and H). The largest discrepancy between the 2×2 mesh and the fine mesh results was 52 %, which occurred in the steel decking, at point F. Note that the temperature of the decking remains significantly below the gas temperature for times between 20 min and 50 min, when the largest discrepancies are observed (compare Figure 3–15(f) and Figure 3–13(b)), as a result of heat transfer through the decking into the concrete slab. Refinement of the mesh significantly affects the temperature at point F because of this heat transfer into the concrete slab. Refining the mesh reduced the maximum discrepancy to 31 % for the 4×4 mesh (at point F) and to 19 % for the 8×8 mesh (at point A). The discrepancy was always largest in the steel decking, and for the 4×4 and 8×8 meshes, it is noted that the maximum discrepancy occurred within the first 40 minutes of heating, with a discrepancy of less than 5 % thereafter. Better agreement was observed at the top surface of the slab, with a maximum discrepancy of 8 % at point E for the 4×4 mesh. The mesh refinement study thus showed that the 4×4 mesh (Figure 3–14b) yielded reasonable accuracy for the temperature distribution in the slab, with an underestimation of the temperature in the steel decking by up to 31 % in the initial 40 minutes of heating and a maximum discrepancy of 8 % thereafter.

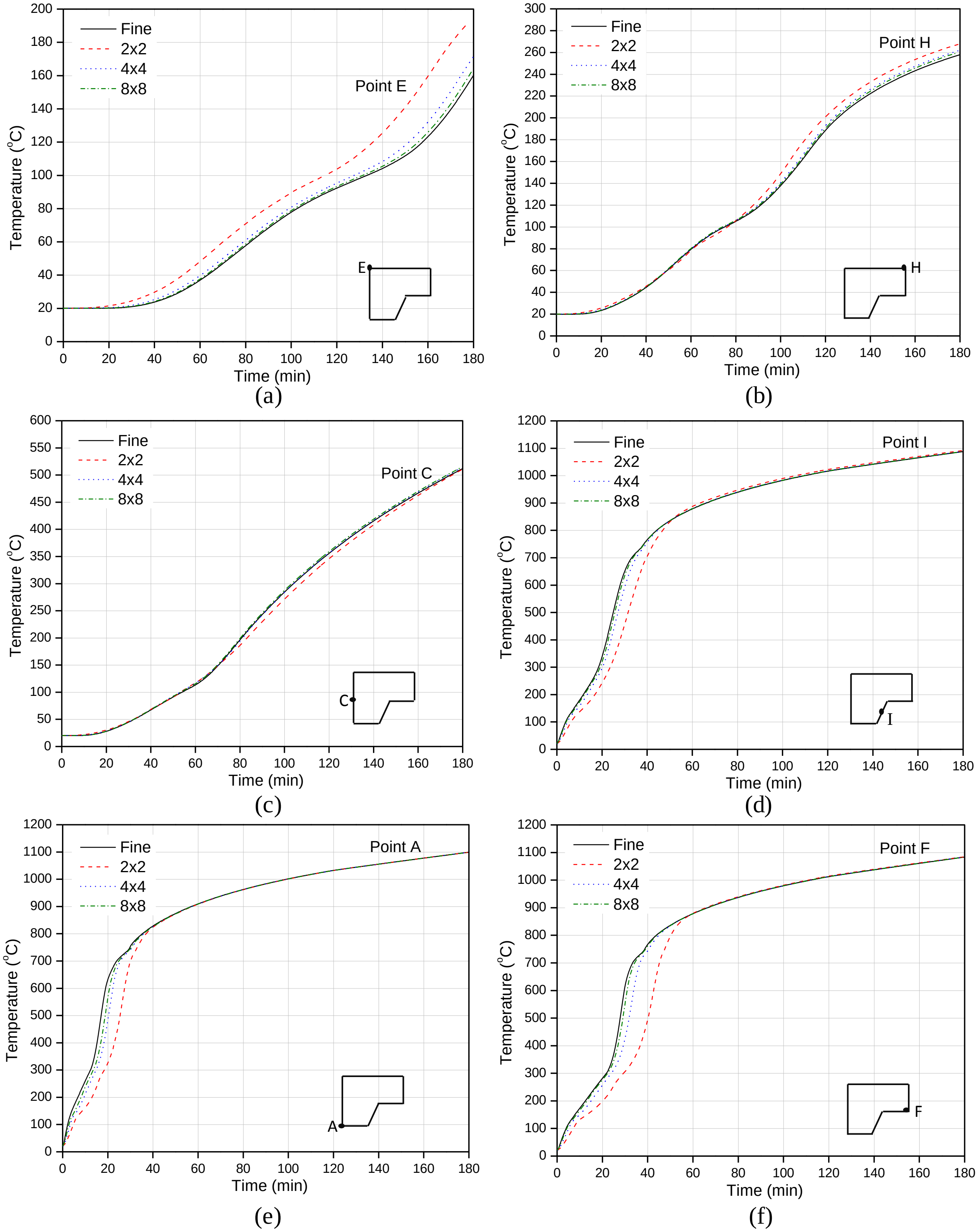

Figure 3–15. Comparison of temperature histories for fine mesh and for three alternative coarse meshes: (a) point E; (b) point H; (c) point C; (d) point I; (e) point A; (f) point F

3.5 SUMMARY

This chapter presented the development of a detailed modeling approach for thermal behavior of composite slabs. The performance of the detailed model was validated against experimental results. A summary of key findings is provided below:

- A temperature-dependent emissivity of the galvanized steel decking should be considered which may affect the temperature distribution in composite slabs. A new model was proposed in this study where the emissivity was taken as 0.1 and 0.7 at temperatures below 400 °C and above 800 °C, respectively, with a linear variation between 0.1 and 0.7 for temperatures between 400 °C and 800 °C.
- The presence of ribs resulted in a non-uniform temperature distribution along any horizontal plane in the upper continuous portion of the slab. It was found that the web and upper flange of the decking had a slightly lower temperature than the lower flange due to the shielding effect of the rib. Due to the large heat capacity of the concrete slab, the temperature of the steel decking is significantly lower than the gas temperature in the early stages of heating but converges to the gas temperature in the later stages.
- The mesh sensitivity study showed that a 4×4 mesh (4 elements along the width of decking flanges and 4 elements along the height of rib and upper flat portion, respectively) yielded reasonable accuracy for the temperature distribution in the slab.

Chapter 4
PARAMETRIC STUDY

This chapter describes a parametric study using the detailed modeling approach described in Chapter 3. The influences of thermal boundary conditions, thermal properties of the materials, and slab geometry on the temperature distribution in composite slabs were studied. Section 4.1 describes the baseline configuration for the prototype composite slab. Section 4.2 describes the effect of thermal boundary conditions, including the heat input from the steel decking and its view factor, while Section 4.3 describes the effect of thermal properties of concrete. Various definitions of temperature-dependent conductivity and specific heat in the EC4 (CEN 2005) and ASCE Manual (ASCE, 1992) were used to investigate the influence of these parameters on the temperature distribution in composite slabs. Section 4.4 describes the effect of slab geometry by varying the five lengths (h_1, h_2, l_1, l_2, and l_3) illustrated in Figure 2–2. Finally, Section 4.5 presents a summary of the findings from the parametric study.

4.1 PRACTICAL RANGES FOR COMPOSITE SLAB DIMENSIONS

The detailed modeling approach proposed in Chapter 3 was used to perform parametric studies on the thermal behavior of composite slabs. The fine mesh shown in Figure 3–1 was used throughout this chapter. The typical composite slab configuration illustrated in Figure 3–12, with Vulcraft 3VLI decking, was selected as the baseline configuration for this parametric study. The 3VLI decking has a thickness of 0.9 mm. Lightweight concrete was used for all the models in this Chapter, except where specifically noted, due to its common usage in practice. The following baseline modeling parameters were adopted in the numerical analyses: (1) the ISO 834 standard fire curve (International Organization for Standardization, 2014) was used to determine the gas temperature at the fire-exposed surface of the slabs; (2) the convective heat transfer coefficient was taken as 25 W/(m^2·K) for the lower flange and 15 W/(m^2·K) for the web and the upper flange, to consider the shielding effect of the ribs; a value of 8 W/(m^2·K) was taken for the unexposed surface of the slab; (3) a temperature-dependent emissivity of steel based on Hamerlinck *et al.* (1990) was used (0.1 for T < 400 °C and 0.4 for T > 800 °C), see Chapter 3; (4) the view factor for the upper flange and web was calculated based on Eq. (2.3); (5) The moisture content was taken as 5 % for lightweight concrete, which determined the specific heat (see Section 2.3); and (6) the thermal properties of the concrete were adopted from the EC4 (using the upper limit for the thermal conductivity).

A survey was conducted on recent experimental and numerical studies on composite slabs, as shown in Table 4–1. The parameters Φ_{up} and α are the view factor of the upper flange and the angle of the web, respectively, as defined in EC4. Table 4–2 shows a practical range of parameters h_1, h_2, l_1, l_2, and l_3 based on the survey shown in Table 4-1. Considering the practical ranges of geometric parameters, the parametric study used values of h_1 = (50 mm, 85 mm, 125 mm), h_2 = (50 mm, 75 mm, 100 mm), l_1 = (130 mm, 184 mm, 250 mm), l_2 = (80 mm, 120 mm, 160 mm), and l_3 = (80 mm, 120 mm, 160 mm). Only one geometric parameter was changed at a time, with all other parameters having the values shown in Figure 3–12.

Table 4–1. Summary of composite slab properties from previous studies (see Figure 3-12)

Reference	Type of Decking	Slab Dimensions (mm)					Φ_{up}	α
		h_1	h_2	l_1	l_2	l_3		(°)
TNO Tests (Hamerlinck et al. 1990)	Prins PSV 73	70	73	84	47	20	0.36	76
	PMF CF 60	70	60	169	120	131	0.78	68
	Cofrastra 70	75	70	113	87	70	0.53	80
	Ribdeck 60	60	90	185	155	115	0.58	81
Cardington tests (Kirby 1997)	PMF CF70	70	60	188	136	112	0.76	67
Bailey et al. (2000)	PMF F60	90	60	136	90	64	0.65	69
Tongji Tests (Li and Wang 2013)	-	70	76	202	142	142	0.75	68
BRANZ (Lim et al. 2004)	Hibond	75	55	182	130	126	0.80	65
Wellman et al. (2011)	Vulcraft 1.5VLR	64	38	108	88	44	0.61	75
Guo and Bailey (2011)	PMF CF60	85	60	169	120	131	0.78	68
COSSFIRE (Zhao et al. 2011)	COFRAPLUS 60	97	58	101	62	107	0.73	71
Main and Sadek (2012)	Vulcraft 3VLRI	83	76	172	132	132	0.69	75
Bednar et al. (2013)	TR40/160	40	38	110	50	50	0.80	52
Pantousa et al. (2013)	-	77	73	96	50	92	0.65	73

Table 4–2. Practical ranges for dimensions of composite slabs

h_1 (mm)	h_2 (mm)	l_1 (mm)	l_2 (mm)	l_3 (mm)	Thickness of deck (mm)	Φ_{up}	A/L_r (mm)	α (°)
50~125	40~100	60~200	32~160	40~150	0.7~1.2	0.2~0.8	20~50	45~90

4.2 INFLUENCE OF THERMAL BOUNDARY CONDITIONS

As shown in Eq. (2.2), the convection and radiation boundary conditions are represented by the convective heat transfer coefficient h_c, the emissivity of the surface material ε_s (galvanized steel on the fire-exposed side and concrete on the unexposed side), and the view factor Φ. In this section, the sensitivity of temperature rise in composite slabs to these three parameters is studied. In addition, the influence of heat input through different surfaces of the steel decking (lower flange, upper flange, and web) is also examined.

4.2.1 Influence of Convective Heat Transfer Coefficient

For the convective heat transfer coefficient of the fire-exposed side of composite slabs, the EC4 (CEN 2005) recommends a value of 25 W/(m²·K) for a standard fire and 35 W/(m²·K) for a natural fire. Hamerlinck *et al.* (1990) suggested a smaller coefficient of 15 W/(m²·K) for the web and upper flange of the decking to consider the reduced rate of heat flux in the void between two consecutive webs. Figure 4–1 shows the variation of temperatures in the thick and thin portions of slabs for convective heat transfer coefficients in the range of 15 W/(m²·K) to 35 W/(m²·K). The figure indicates that the convective heat transfer coefficient has little effect on the temperature distribution in the slab except for at the steel decking (points A and F) during the early stages of heating. The upper flange of the deck (point F) is more sensitive to the coefficient than the lower flange (point A) due to its smaller view factor. As the convective heat transfer coefficient has a minimal influence on deck temperatures in the later stages of heating, its influence on the fire-exposed side can be considered negligible.

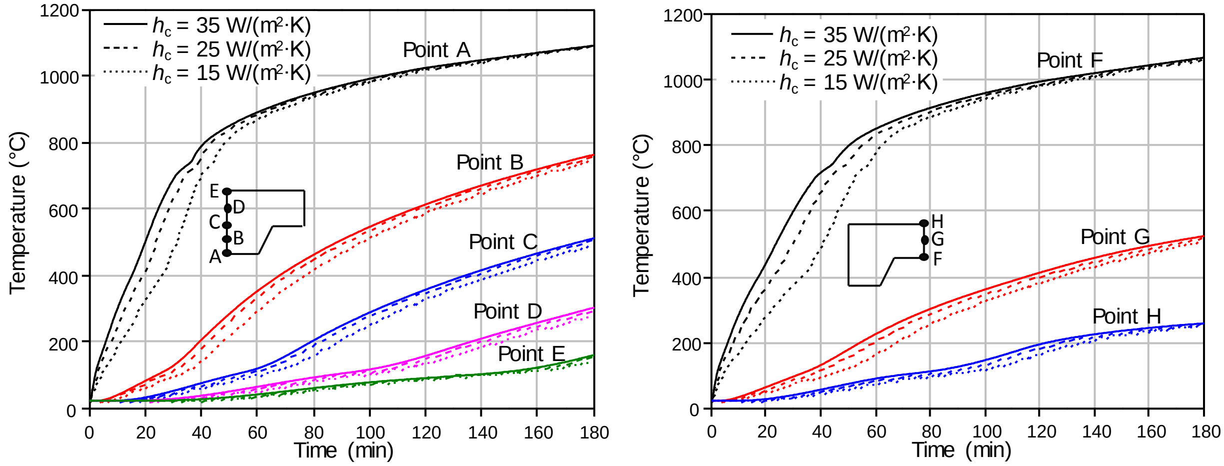

(a) (b)

Figure 4–1. Temperature histories within composite slabs with varying convective heat transfer coefficient for the fire-exposed surface: (a) thick portion of slab; (b) thin portion of slab.

For the convective heat transfer coefficient for the unexposed side of composite slabs, EC4 recommends a value of 4 W/(m^2·K) when heat transfer by radiation is considered, and 9 W/(m^2·K) when heat transfer by radiation is not considered. Hamerlinck *et al.* (1990) suggested a coefficient of 8 W/(m^2·K) for the unexposed side, while considering radiation effects. Figure 4–2 shows the variation of temperatures in the thick and thin portions of the slab for varying coefficients of heat transfer by convection of the unexposed side. The convective heat transfer coefficient was taken as 25 W/(m^2·K) for the lower flange and as 15 W/(m^2·K) for the web and upper flange. In general, the temperature distribution in the slab was not sensitive to the boundary condition at the unexposed surface. Only Point H, located at the unexposed surface of the thin portion of the slab, exhibited a noticeable sensitivity to the boundary condition at the unexposed side.

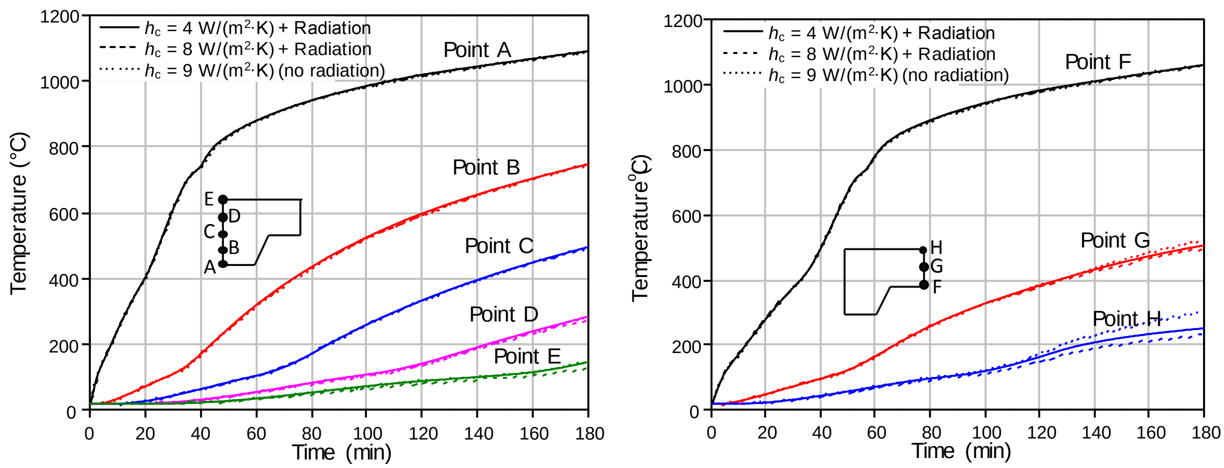

(a) (b)

Figure 4–2. Temperature histories within composite slabs with varying convective heat transfer coefficient for the unexposed surface: (a) thick portion of slab; (b) thin portion of slab.

4.2.2 Influence of Emissivity

EC4 recommends a value of 0.7 for the emissivity of steel decking of composite slabs. Hamerlinck *et al.* (1990) suggested a temperature-dependent emissivity of 0.1 for T ≤ 400 °C and 0.4 for T ≥ 800 °C to account for melting of the zinc-layer on the decking. Figure 4–3 shows the variation of temperature distribution in the slab with a constant emissivity of 0.1, 0.4, and 0.7 for the steel decking (lower flange, web, and upper flange). When compared to the limited effect of the convective heat transfer coefficient for the fire-exposed side of the slab in Figure 4–1, the emissivity of steel had significant influence on the temperature rise in the slab. At a given time, the temperatures at Points A~F decreased with lower emissivity. This decrease is more pronounced for values of emissivity between 0.1 and 0.4 than for values between 0.4 and 0.7.

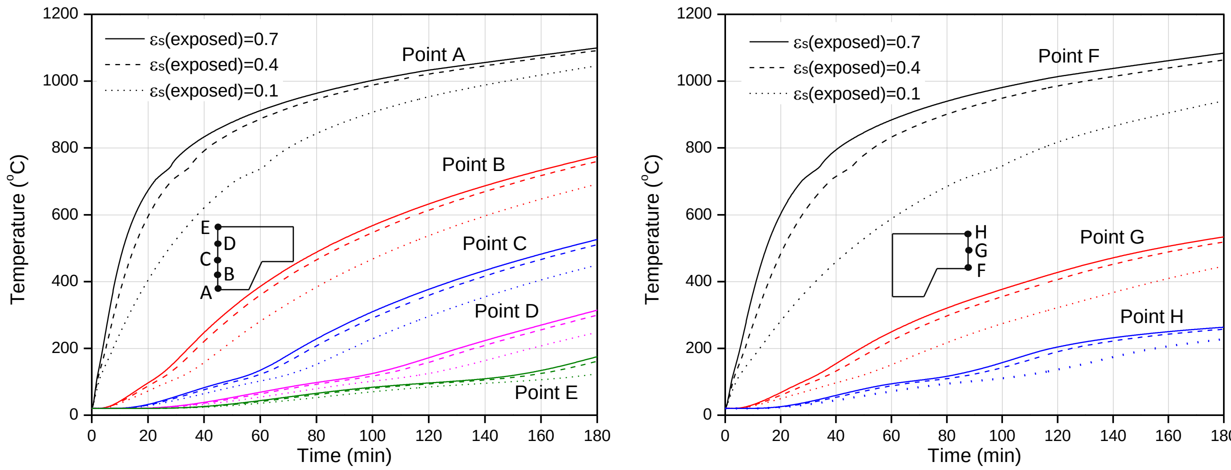

(a) (b)

Figure 4–3. Temperature histories within composite slabs with different temperature-independent values for the emissivity of galvanized steel: (a) thick portion of slab; (b) thin portion of slab

Figure 4–4 shows a comparison of temperature distribution in the slab with constant (0.7 based on EC4) and temperature-dependent emissivity of steel decking based on Hamerlinck *et al.* (1990), and the proposed emissivity in Eq. (3.1) (see Section 3.2.1). The temperature-dependent emissivity resulted in lower temperatures during the early stages of heating, especially for the steel decking (Points A and F). In general, the two temperature-dependent models of emissivity produced similar temperature histories, except for the temperature of the steel decking (Points A and F). The proposed model for emissivity in Eq. (3.1) predicted higher temperatures in the steel decking than those produced by the Hamerlinck *et al.* (1990) model.

The emissivity of concrete at the unexposed surface of slabs is recommended as 0.7 in EC4 and 0.8 in EN 1991-1-2 (CEN 2009). Hamerlinck *et al.* (1990) suggested a value of 0.78. Figure 4–5 shows that the practical range of concrete emissivity of 0.6 to 0.8 had a negligible influence on the temperature rise in composite slabs. From Figures 4–2 and 4–5, it can be seen that the thermal boundary conditions on the unexposed side had little to no influence on the temperature distribution in composite slabs.

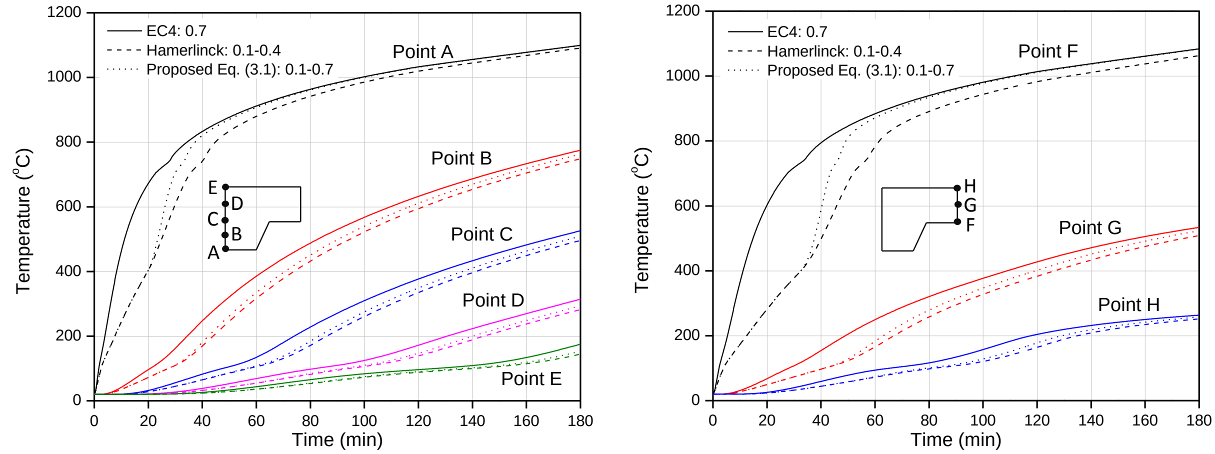

(a) (b)

Figure 4–4. Temperature histories within composite slabs with different temperature-dependent models for the emissivity of galvanized steel: (a) thick portion of slab; (b) thin portion of slab

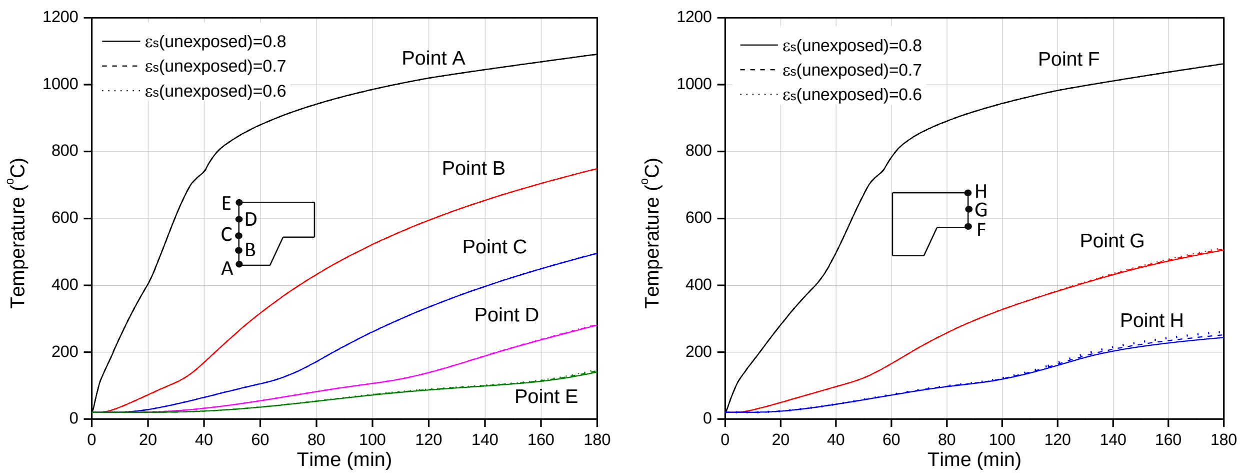

(a) (b)

Figure 4–5. Temperature histories within composite slabs with varying constant emissivity of concrete at unexposed side: (a) thick portion of slab; (b) thin portion of slab

4.2.3 Influence of View Factor

The equations for calculating view factors of the web and upper flange of steel decking were presented in Eq. (2.3). The view factor of the lower flange is always taken as 1.0. Figure 4–6 shows the variation of temperature in composite slabs with view factors of the web, Φ_{web}, having values of 0.2, 0.4, and 0.8. For these analyses, the view factor of the upper flange was calculated from Eq. (2.3) as $\Phi_{up} = 0.73$. The view factor, Φ_{web}, significantly affected the temperature of the web (Point I) but had a negligible effect on the temperatures in the concrete. Figure 4–7 shows the results for varying the view factor of the upper flange, Φ_{up}, with values of 0.2, 0.4, 0.8. For these analyses, the view factor of the web was calculated from Eq. (2.3) as $\Phi_{web} = 0.59$. Similar to the previous observations for the emissivity of steel, the temperatures in the thin portion of the slab were sensitive to the view factor of the upper flange, Φ_{up}, while the temperatures in the thick portions were not.

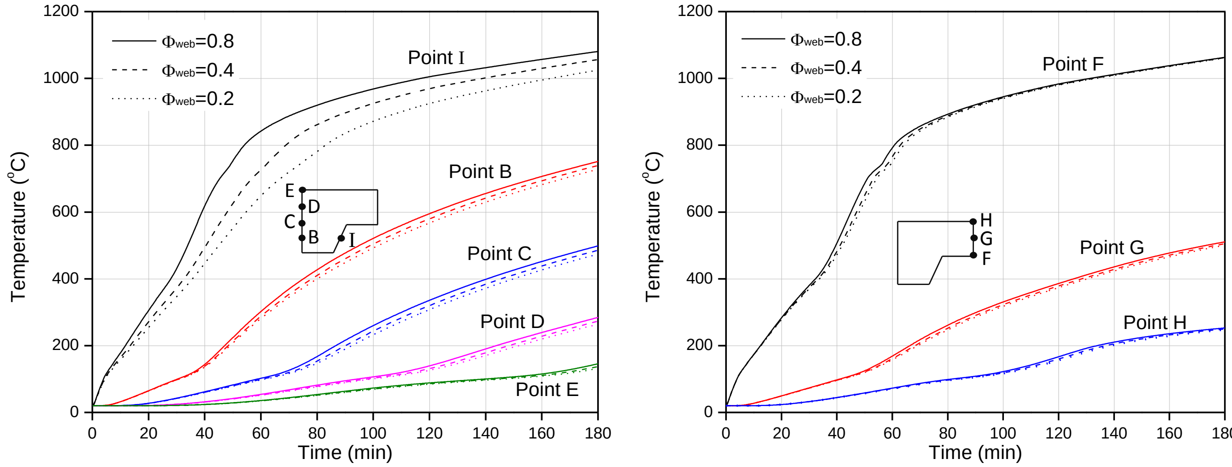

(a) (b)

Figure 4–6. Temperature histories within composite slabs with varying Φ_{web}: (a) thick portion of slab; (b) thin portion of slab

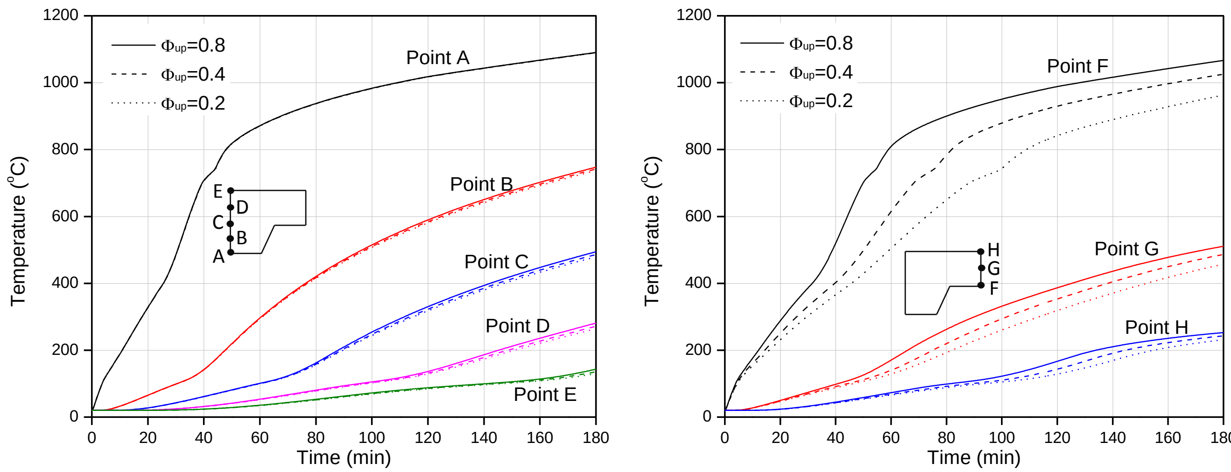

(a) (b)

Figure 4–7. Temperature histories within composite slabs with varying Φ_{up}: (a) thick portion of slab; (b) thin portion of slab

Table 4–3 presents a comparison of fire resistance values obtained from the numerical analysis with different values of Φ_{up}. As in EC4 (CEN 2005), the fire resistance, expressed in minutes, is based on the fire duration until a maximum temperature rise of ΔT=180 °C or an average temperature rise of ΔT=140 °C, whichever governs, is reached at the unexposed surface of the slab. Table 4–3 shows that the maximum temperature rise criterion governed the fire resistance of the composite slabs. The fire resistance was sensitive to the view factor of the upper flange.

Table 4–3**.** Comparison of fire resistance values obtained from numerical analyses for different view factors of the upper flange, Φ_{up} (governing values in bold)

View factor of upper flange, Φ_{up}	Fire resistance (min), based on:	
	Max. temp.	Ave. temp.
0.2	**155**	157
0.4	**145**	149
0.8	**134**	140

4.2.4 Influence of Heat Input Through Decking

For composite slabs, the boundary conditions (i.e., convection and radiation) should be specified on the lower flange, web, and upper flange of the steel decking, as well as at the unexposed surface of the slab, as shown in Figure 3–1. The temperature distribution within the slab is significantly affected by the input of thermal energy through the steel decking. Figure 4–8 shows the temperature contours in the slab after 180 min of heating for different combinations of heat input from the lower flange, web, and upper flange. The gas temperature (from ISO 834 standard fire curve) at this time (180 min) was 1383 °C. The temperature in the rib was primarily influenced by heat transfer through the lower flange and web (Figure 4–8c). The temperature distribution in the upper continuous portion of the slab (i.e., the portion of the slab above the top of the steel decking) was governed by heat input through the upper flange (Figure 4–8d). These behaviors can be seen more clearly in Figure 4–9, which shows a comparison of temperature histories within composite slabs for thermal loading on different surfaces. The temperature of the lower flange was governed by the heat transfer through the lower flange and approached the gas temperature in the later stages of heating (Figure 4–9a). The heat input through the upper flange had a significant influence on the temperature in the rib (Figures 4–9b and c). This effect was more pronounced in the middle of the slab (Point C) than at the bottom of the rib (Point B) or the top of the slab (Point E). For the upper continuous portion of the slab, the heat input through the web had a greater influence on the temperature distribution than the heat input through the upper flange (Figure 4–9c and d). The heat input through the upper flange dominated the temperature distribution in the thin portion of the slab, with heat input through the lower flange and the web having a much lesser effect (Figures 4–9e and f).

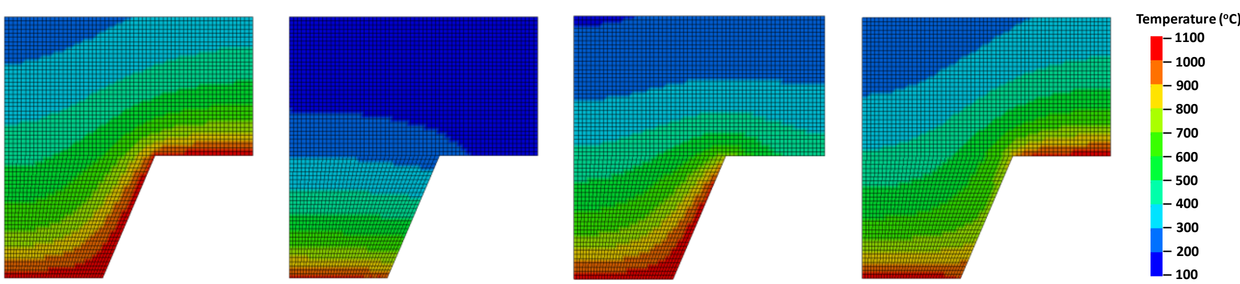

(a) (b) (c) (d)

Figure 4–8. Temperature contours at 180 min for thermal loading on different surfaces: (a) all decking surfaces, (b) lower flange, (c) lower flange and web, (d) lower flange and upper flange

Due to the presence of ribs, the temperatures of the upper continuous portion of the slab varied along a given horizontal plane by more than 100 °C (see Figure 4–8a). The temperature distribution in the rib was also non-uniform along a given horizontal plane due to the influence of heat input from the web. The complex temperature distribution in composite slabs poses challenges to determining the temperature of the reinforcement placed within the rib or above the rib. The thermal loading is applied on all the surfaces of the steel decking in a detailed model. This is not the case, however, for reduced-order model using layered shell elements, as proposed in Chapter 5, for which heat input through the web of the decking cannot be directly modeled. Methods to account for heat input through the web of the decking within the reduced-order modeling approach are presented in Chapter 5.

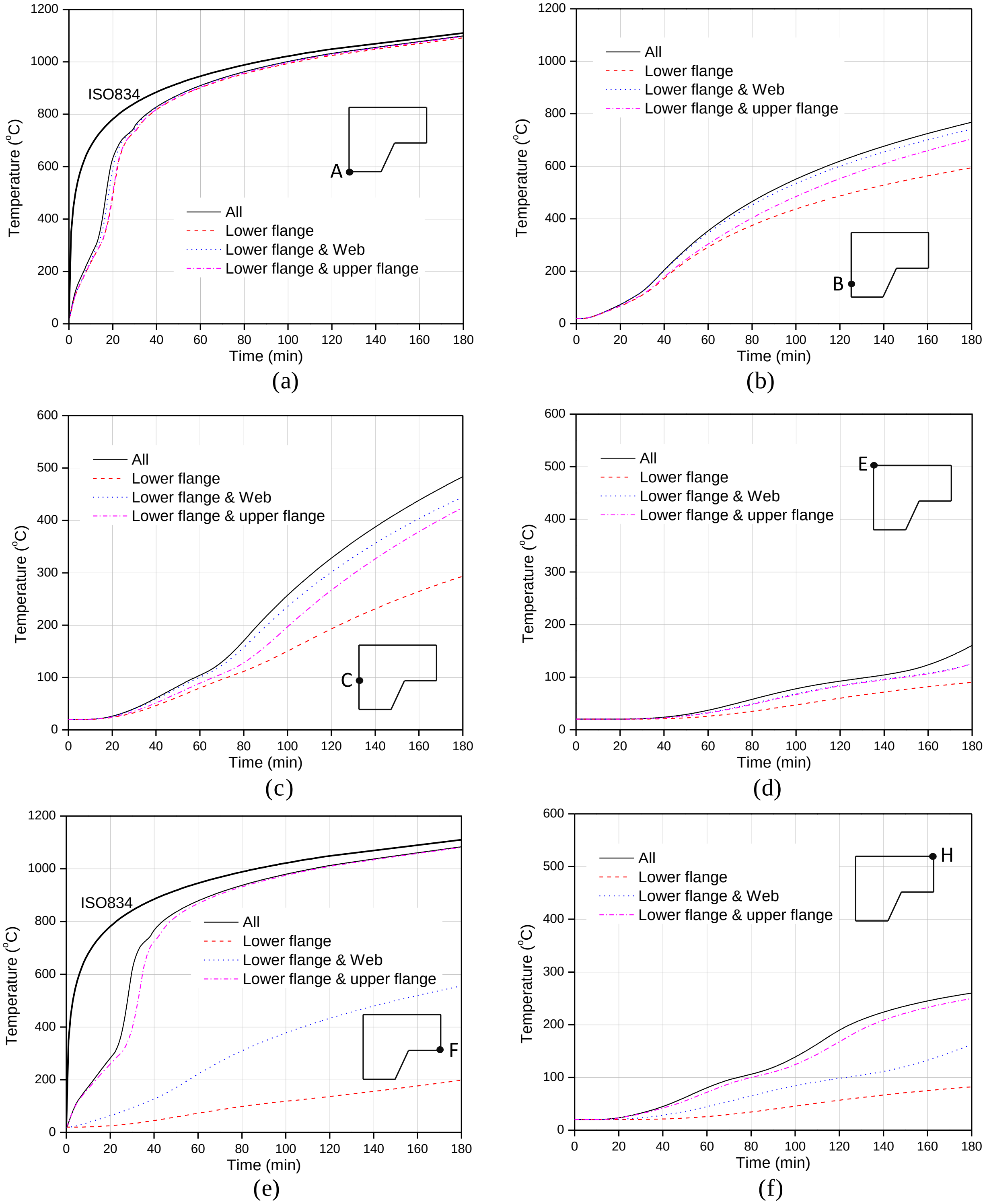

Figure 4–9. Comparison of temperature within composite slabs for thermal loading on different surfaces: (a) Point A; (b) Point B; (c) Point C; (d) Point E; (e) Point F; (f) Point H

4.3 INFLUENCE OF THERMAL PROPERTIES OF CONCRETE

The temperature rise in composite slabs depends on the thermal properties of concrete, including thermal conductivity, and specific heat. The density of concrete is considered independent of temperature and is taken as 2300 kg/m^3 for normal-weight concrete and 1900 kg/m^3 for lightweight concrete in EC4 (CEN, 2005). The thermal conductivity and specific heat vary with moisture content and aggregate type, as discussed previously in Section 2.4. Temperature-dependent expressions for these two properties are given in EC4 and in the ASCE manual on structural fire protection, as shown in Figure 2–3 and Figure 2–4. The ASCE manual distinguishes between siliceous and carbonate aggregates, while EC4 applies to all aggregate types. The influences of the thermal conductivity and specific heat on the temperature distribution in composite slabs are presented in the following sections.

4.3.1 Influence of Thermal Conductivity

There are significant differences in the temperature-dependent models for the thermal conductivity of concrete given in EC4 and in the ASCE manual, as shown in Figure 2–4. The data from Kodur (2014) are generally higher than the upper-limit model in EC4. To envelope the data, a new upper bound is proposed in this study by assuming linear variation in the conductivity from 2.5 W/(m·K) at 20 °C to 1.25 W/(m·K) at 800 °C, with a constant conductivity of 1.25 W/(m·K) above 800 °C. A set of analyses was performed using the various models for the thermal conductivity of concrete given in EC4 and in the ASCE manual, as well as the newly proposed upper bound. In these analyses, the specific heat of normal-weight concrete was estimated based on an assumed moisture content of 3 %, and the temperature-dependent model of Hamerlinck *et al.*, (1990) was used for the emissivity of the galvanized steel decking (see Section 2.3).

Figure 4–10 shows a comparison of temperature histories in the slab obtained using the various models for thermal conductivity of normal-weight concrete. Generally, the thermal conductivity of concrete had a larger effect on the temperatures at the unexposed side (points E and H) than on the temperatures at the fire-exposed side (points A and F). Predictions based on the upper-limit model in EC4 typically fell between the predictions based on the lower-limit model in EC4 and the proposed upper bound. Predictions based on the two ASCE models were similar to each other and also to predictions based on the upper-limit model in EC4. Table 4–4 shows a comparison of the fire resistance values obtained from numerical analyses using the various models for the thermal conductivity of normal-weight concrete. In all cases, the fire resistance was governed by the maximum temperature criterion, rather than the average temperature criterion (see Section 4.2.3). Since the experimental conductivity values from Kodur (2014) exceeded the EC4 upper limit, use of either the proposed upper bound or the EC4 upper limit would be required to avoid overestimation of the fire resistance. For lightweight concrete, the fire resistance values obtained from numerical analysis using the EC4 and ASCE models (see Figure 2–4) were 125 min and 121 min, respectively, both of which were governed by the maximum temperature criterion.

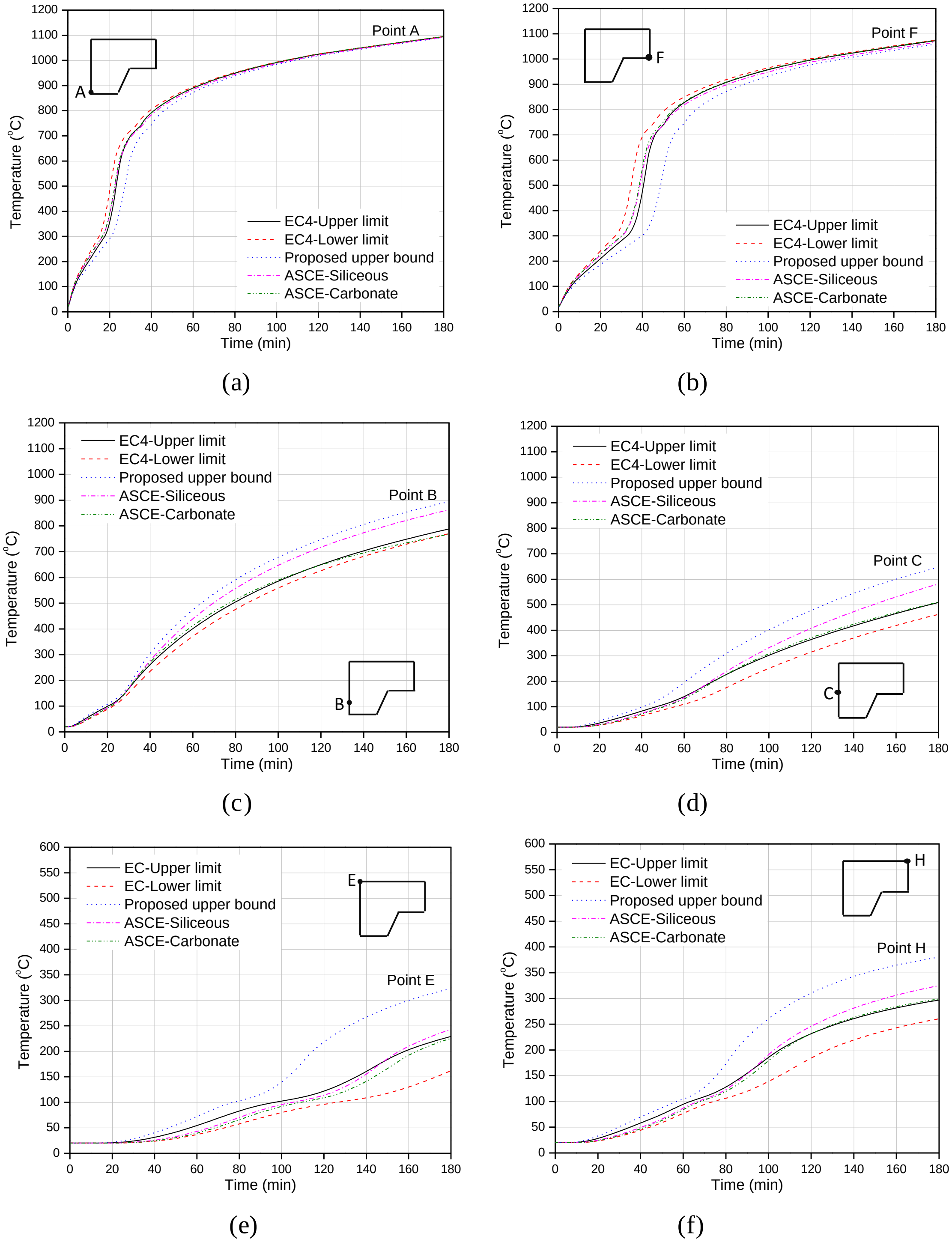

Figure 4–10. Temperature histories within composite slabs with different models for concrete conductivity: (a) Point A; (b) Point F; (c) Point B; (d) Point C; (e) Point E; (f) Point H

Table 4–4. Comparison of fire resistance values obtained from numerical analyses with different models for thermal conductivity of normal-weight concrete (governing values in bold)

	Fire Resistance (min), based on:	
Thermal Conductivity Model	Max. temp.	Ave. temp.
EC4 upper limit	**105**	110
EC4 lower limit	**128**	136
Proposed upper bound	**85**	88
ASCE siliceous	**103**	110
ASCE carbonate	**107**	114

4.3.2 Influence of Specific Heat

Figure 2–3 shows the two models (EC4 and ASCE) for the specific heat of concrete. For dry (zero moisture content) normal-weight concrete, constant values of 1000 J/(kg·K) and 1170 J/(kg·K) are recommended for simple calculations in EC4 and in the ASCE manual, respectively (see Figure 2–3a). A constant specific heat of 840 J/(kg·K) is recommended for lightweight concrete in EC4. EC4 also recommends a temperature-dependent model for specific heat of dry normal-weight concrete, whereby the specific heat varies between 900 J/(kg·K) and 1100 J/(kg·K), see Section 3.3.2 of Annex D. Figure 4–11 shows the variation of temperature in the slab when constant values of 1000 J/(kg·K) and 1170 J/(kg·K) are used, as well as the temperature-dependent model from EC4. The temperatures within the slab for the constant specific heat of 1000 J/(kg·K) agree well with the temperature-dependent model.

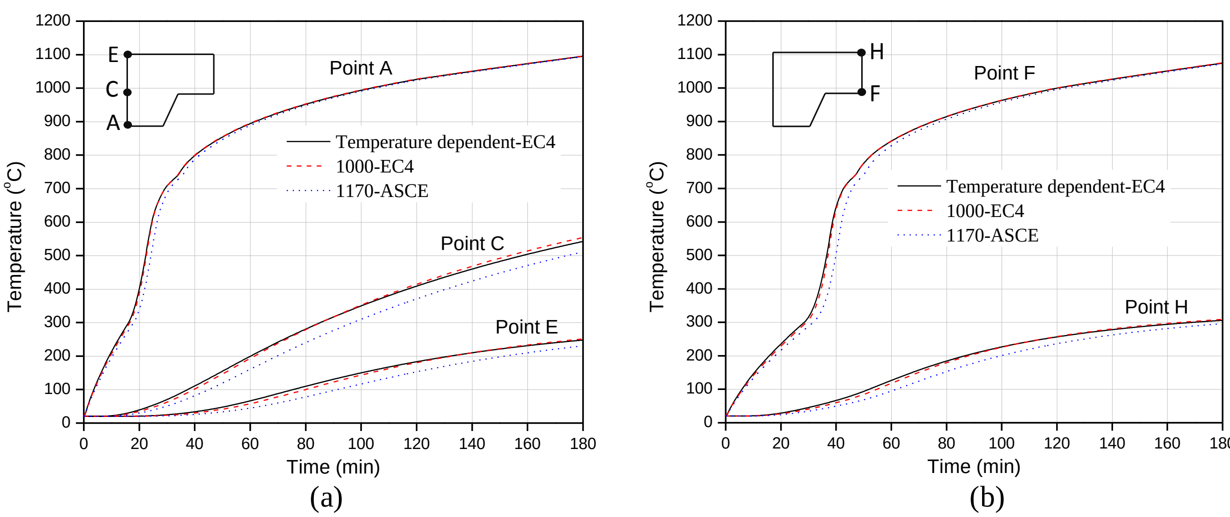

Figure 4–11. Temperature histories within composite slabs with varying specific heat (dry normal-weight concrete): (a) thick portion of slab; (b) thin portion of slab

To account for the influence of moisture content (m.c.) of normal-weight concrete on the thermal response of the slabs, the analyses accounted for the spike in the specific heat for temperatures between 100 °C and 200 °C, Figure 2–3a. The moisture content had a significant influence on the temperatures in the slab, as shown in Figure 4–12, especially at the unexposed surface (Point E), where a reduction in the rate of temperature increase was evident as the temperature passed through 100 °C. This effect was more significant for higher values of moisture content, leading to greater delays in the temperature rise within the concrete, and a plateau in the temperature history is clearly evident in Figure 4–12b for the moisture content of 7 %. After most of the moisture had evaporated (at temperatures exceeding about 150 °C), a more rapid rise in the concrete temperature was evident.

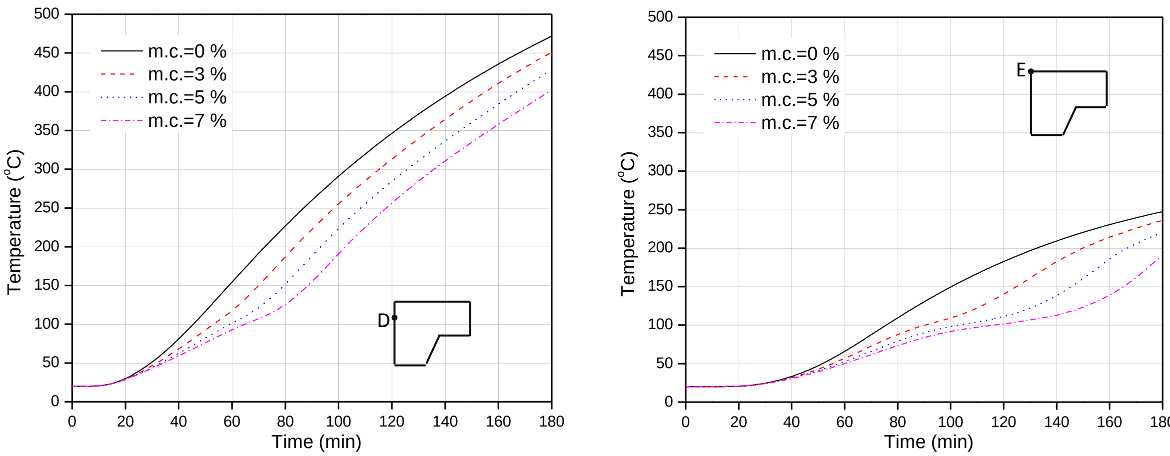

(a) (b)

Figure 4–12. Temperature histories within composite slabs with varying moisture content: (a) Point D; (b) Point E

A comparison of fire resistance between numerical results for both lightweight concrete and normal-weight concrete is shown in Table 4–5. Values of specific heat for normal-weight and lightweight concrete were based on Figure 2–3a and Figure 2–3b, respectively, for moisture content values of 0 %, 3 %, 5 %, and 7 %. Interpolation was used to calculate the peak specific heat for moisture contents of 5 % and 7 %. The numerical results show that an increment of 1 % in moisture content led to an enhancement of the fire resistance by about 5 minutes.

Table 4–5. Comparison of numerical results for fire resistance of slabs with different values of moisture content (governing values in bold)

Type of Concrete	Moisture Content	Fire Resistance (min), based on:	
		Max. temp.	Ave. temp.
Normal-weight	0 %	87	**85**
Normal-weight	3 %	**99**	102
Normal-weight	5 %	**110**	117
Normal-weight	7 %	**122**	131
Lightweight	0 %	**96**	98
Lightweight	3 %	**112**	120
Lightweight	5 %	**125**	137
Lightweight	7 %	**138**	153

4.4 INFLUENCE OF SLAB GEOMETRY

The geometry of a composite slab can be represented by the five dimensions illustrated in Figure 3–12: h_1, h_2, l_1, l_2, and l_3, which denote, respectively, the height of the upper continuous portion of the slab, the height of the rib, the width at the top of the rib, the width of the lower flange of the decking, and the width of the upper flange of the decking. The influences of these dimensions on the temperature distribution in the composite slab are discussed in the following subsections.

4.4.1 Influence of h_1

The most significant geometrical factor influencing the fire resistance of composite slabs is the height of the upper continuous portion of the slab, h_1. Numerical analyses were conducted for three slabs with h_1 = (50 mm, 85 mm, and 125 mm). Temperature contours for the three cases are shown in Figure 4–13, and Figure 4–14 shows corresponding temperature histories in the thick and thin portions of the slabs. The dimension h_1 had the greatest influence on the temperature of the unexposed surface of the slab, especially in the thin portion (points G and H in Figure 4–14b). For the largest value of h_1 = 125 mm, plateaus are clearly evident in the temperature histories at points E and H as the temperature passes through 100 °C, due to the effect of the increased moisture content associated with the larger concrete mass (see Section 4.3.2).

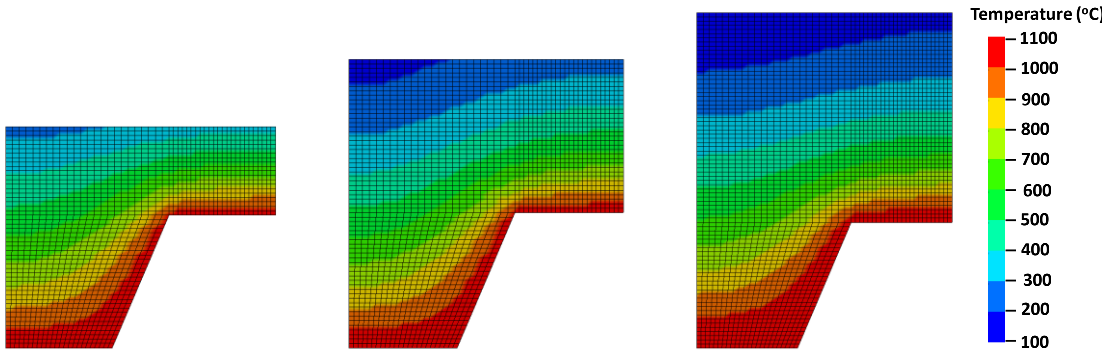

(a) (b) (c)

Figure 4–13. Comparison of temperature contours within composite slabs with varying h_1 after 180 min of heating: (a) h_1 = 50 mm; (b) h_1 = 85 mm; (c) h_1 = 125 mm

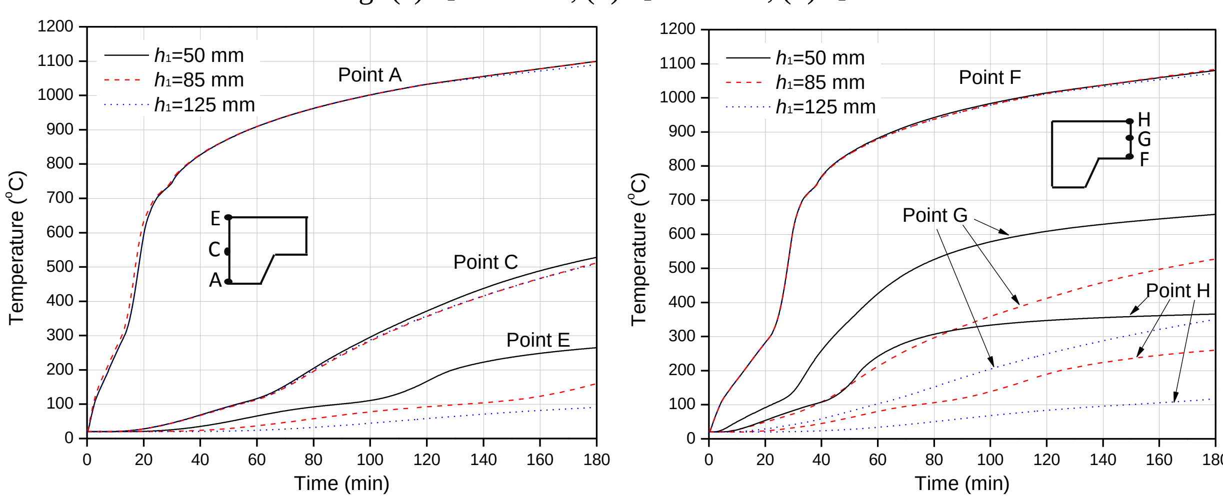

(a) (b)

Figure 4–14. Temperature histories within composite slabs with varying h_1: (a) thick portion of slab; (b) thin portion of slab

4.4.2 Influence of h_2

Three slabs with different rib heights were modeled (h_2 = 50 mm, 75 mm, and 100 mm), and the results are shown in Figures 4–15 and 4–16. As h_2 was increased, the angle of the web increased, resulting in steeper isotherms, as shown in Figure 4–15. Figure 4–16 shows that the increased rib height resulted in reduced temperatures at all locations in the slab except for point A. (The temperature at point A was virtually unaffected by varying h_2.) The reductions in temperature resulted from the increased mass of concrete in the rib, and the most significant reductions in temperature were at point C, at the top of the rib.

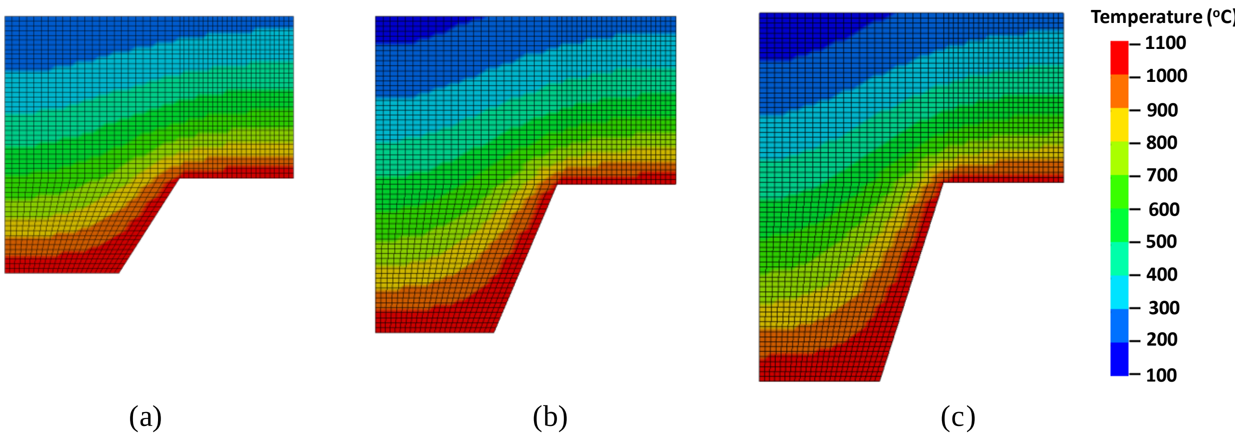

Figure 4–15. Comparison of temperature contours within composite slabs with varying h_2 after 180 min of heating: (a) h_2 = 50 mm; (b) h_2 = 75 mm; (c) h_2 = 100 mm

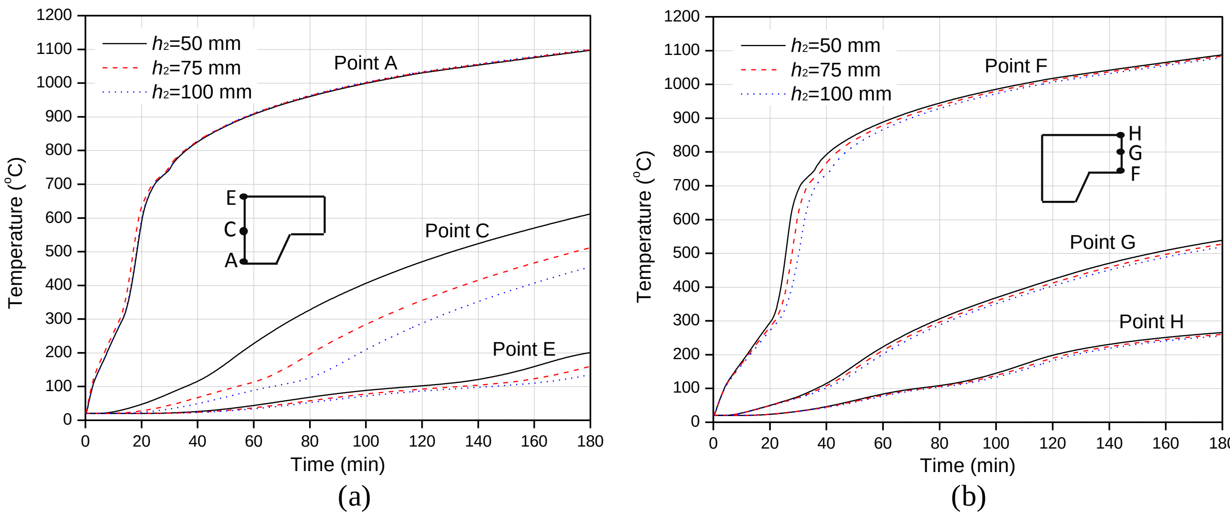

Figure 4–16. Temperature histories within composite slabs with varying h_2: (a) thick portion of slab; (b) thin portion of slab

4.4.3 Influence of l_1

Three slabs with different widths at the top of the rib were studied (l_1 = 130 mm, 184 mm, 250 mm), and the resulting temperature contours and temperature histories in the slab are shown in Figures 4–17 and 4–18, respectively. Increasing l_1 increased the mass of concrete in the rib, which led to a reduction of temperatures in the thick part of the slab (points C and E) and a larger region of cooler temperatures above the rib. However, increasing l_1 had a fairly small effect on the temperatures in the thin portion of the slab (points F, G, and H).

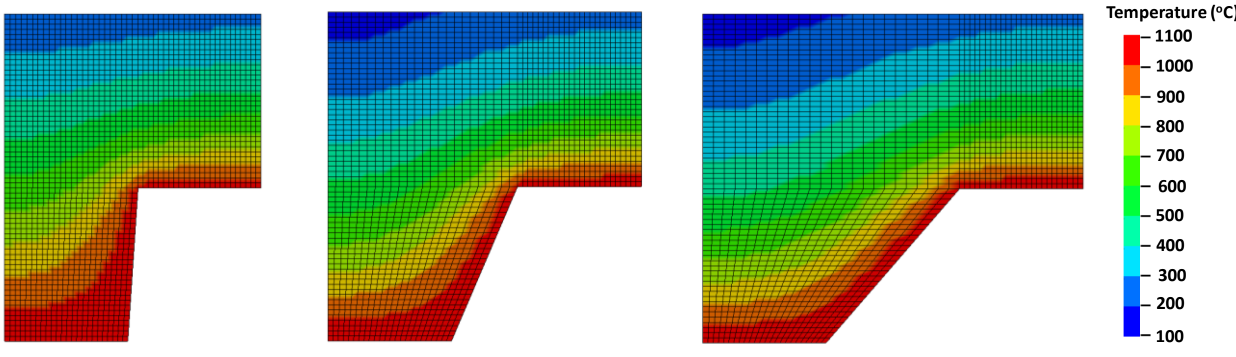

(a) (b) (c)

Figure 4–17. Comparison of temperature contours within composite slabs with varying l_1 after 180 min of heating: (a) l_1 = 130 mm; (b) l_1 = 184 mm; (c) l_1 = 250 mm

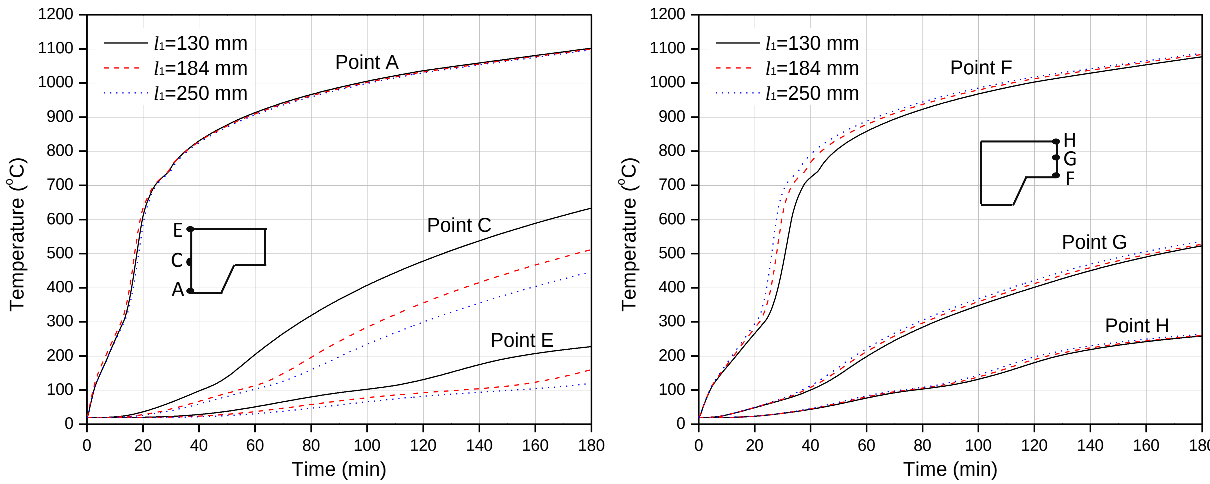

(a) (b)

Figure 4–18. Temperature histories within composite slabs with varying l_1: (a) thick portion of slab; (b) thin portion of slab

4.4.4 Influence of l_2

Three slabs with different widths of the lower flange of the decking were modeled (l_2 = 80 mm, 120 mm, 160 mm), and the resulting temperature contours and temperature histories in the slab are shown in Figures 4–19 and 4–20, respectively. Increasing l_2 increased the mass of concrete in the rib, which led to a reduction of temperatures in the thick portion of the slab (at points C and E), although this effect was less significant than for increases in h_2 and l_1. Increasing l_2 had almost no effect on the temperatures in the thin portion of the slab and only slightly affected the temperature contours in the upper continuous portion of the slab, in spite of the significant changes in the angle of the web.

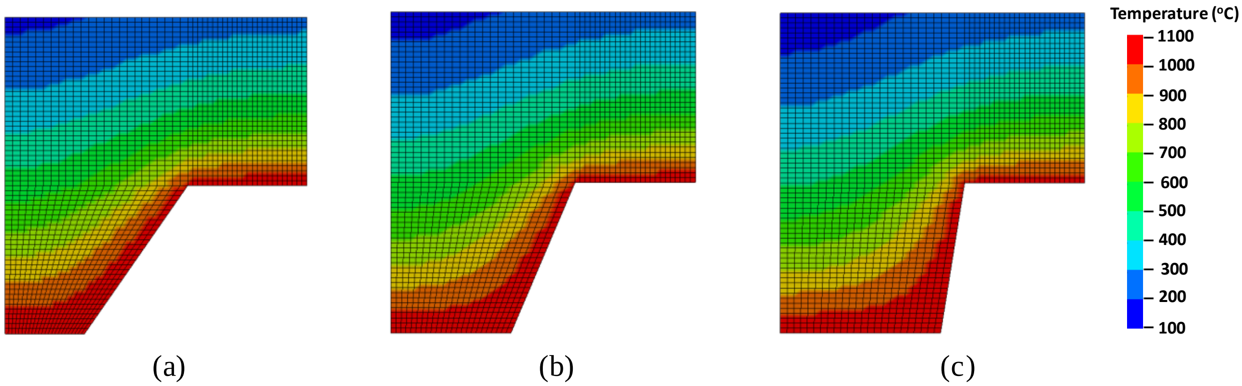

Figure 4–19. Comparison of temperature contours within composite slabs with varying l_2 after 180 min of heating: (a) l_2 = 80 mm; (b) l_2 = 120 mm; (c) l_2 = 160 mm

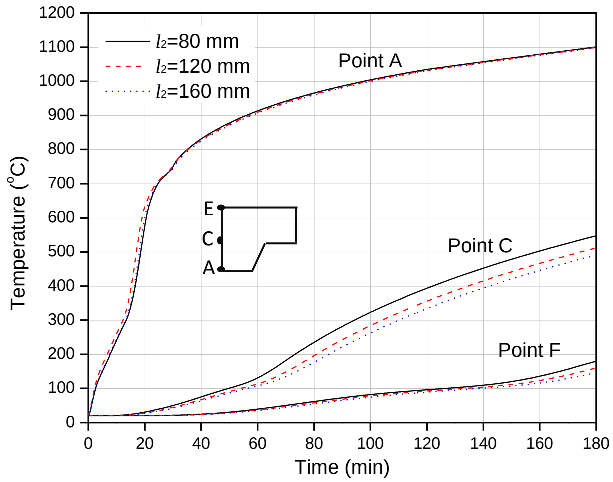

Figure 4–20. Temperature histories within composite slabs with varying l_2

4.4.5 Influence of l_3

The width of the upper flange of the decking, l_3, affects the heat transfer through the thin portion of a composite slab, where the maximum temperature occurs at its unexposed side, but has little influence on the shape of the isotherms for T = 500 °C and the temperature distribution in the thick portion of the slab. Figures 4–21 and 4–22 show, respectively, the computed temperature contours and temperature histories after three hours of heating for three slabs with different upper-flange widths (l_3 = 80 mm, 120 mm, and 160 mm). Although the temperatures in the thin portion of the slab (at points F, G, and H) increased with increasing l_3, this effect was fairly small.

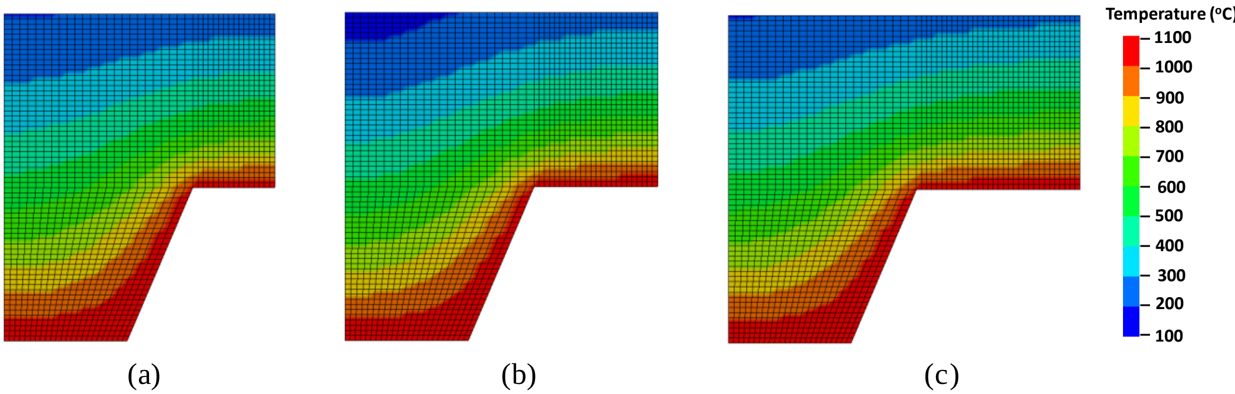

Figure 4–21. Comparison of temperature contours within composite slabs with varying l_3 after 180 min of heating: (a) l_3 = 80 mm; (b) l_3 = 120 mm; (c) l_3 = 160 mm

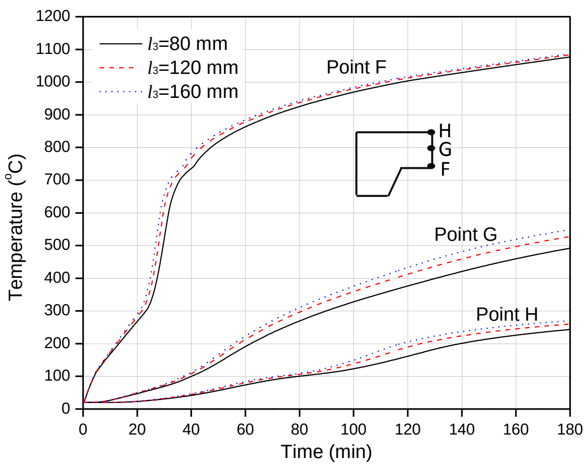

Figure 4–22. Temperature histories within composite slabs with varying l_3

4.5 SUMMARY

This chapter presented a parametric study using the detailed modeling approach presented in Chapter 3. The influence of thermal boundary conditions, thermal properties of the concrete, and slab geometry on the temperature distribution in composite slabs was studied. A summary of key findings is provided below:

- The temperature distribution in composite slabs is highly non-uniform due to the presence of ribs. The heat input through the upper flange of the steel decking governs the temperature distribution in the thin portion of the slab. The temperature distribution in the rib is governed by the heat input through the lower flange and the web of the steel decking. Heat input through both the web and the upper flange of the decking significantly influence the temperature distribution in the upper portion of the slab above the rib. Therefore, the heat input through the web must be considered properly. This is a key challenge for the development of a reduced-order modeling approach that uses shell elements, where only the heat input through the lower and upper flanges can be directly applied, and this challenge is addressed in Chapter 5.
- The thermal conductivity of the concrete had a larger influence on the temperatures at the unexposed surface than the fire-exposed surface. The ASCE models of concrete conductivity are quite similar to the upper limit in EC4, which is recommended for the numerical analysis. The specific heat had less

influence on the temperature than the conductivity, and a constant specific heat value of 1000 J/(kg·K) can be used for simple analytical calculations. The moisture content of the concrete had a significant influence on the temperature distribution. An increase of 1 % in moisture content led to an increase in the fire resistance by about 5 minutes. The fire resistance of composite slabs, based on the thermal insulation criterion at the unexposed surface, was typically governed by the maximum temperature criterion, rather than the average temperature criterion.

- The height of the upper continuous portion of the slab, h_1, was found to be the key geometrical factor influencing heat transfer through the slab, particularly for the thin portion of the slab. Heat transfer through the thick portion of the slab was also significantly affected by the height of the rib, h_2, and the width at the top of the rib, l_1. Increasing h_2 and l_1 led to increasing mass in the rib, which reduced the temperatures in the slab above the rib.

Chapter 5
REDUCED-ORDER MODELING APPROACH

The focus of this chapter is to develop a reduced-order modeling approach for heat transfer analysis of composite slabs that is also suitable for structural analysis, so that the same model can be used for thermal and structural analyses. This chapter describes the development of such a reduced-order modeling approach, calibration and verification of the approach against the detailed models presented in Chapter 3, and validation of the approach against experimental results reported in the literature. Section 5.1 describes the reduced-order modeling approach, which represented the thick and thin portions of a composite slab with alternating strips of shell elements, using a layered thick-shell formulation that accounts for in-plane and through-thickness heat transfer. To account for the tapered profile of the ribs, the layered shell elements representing the thick portion of the slab adopted a linear reduction in the density of concrete with depth in the rib. The layered shell elements representing the thin portion of the slab incorporated a "dummy material" with thickness equal to the height of the rib, so that the thick and thin portions of the slab could be modeled using shell elements with the same thickness, and so that in-plane heat transfer between corresponding layers of adjoining elements could be properly modeled. As described in Section 5.2, modifying the specific heat of the concrete in the ribs was found to be an effective method of indirectly accounting for heat input through the web of the decking, since only thermal loading on the upper and lower flanges of the decking can be explicitly modeled in the layered shell approach. Recommendations are presented for optimal modification of the specific heat of concrete in the rib for slabs with various geometries. Finally, validation of the reduced-order modeling approach is presented in Section 5.3.

5.1 PROPOSED MODELING APPROACH

Use of shell elements in the reduced-order modeling approach enables large-scale structural systems to be analyzed much more efficiently than the detailed approach using solid elements. The proposed reduced-order modeling approach uses a layered composite shell formulation, in which a distinct structural material, thermal material, and thickness can be specified for each layer (*PART_COMPOSITE in LS-DYNA). This allows distinct layers to be specified for the steel decking and the reinforcement, with multiple layers representing concrete specified through the thickness of the slab. A thick thermal shell formulation is used, which allows for both in-plane and through-thickess heat conduction, with thermal gradients through the thickness of each layer. The geometry of the slab is captured using alternating strips of shell elements to represent the thick and thin portions of the composite slab, as illustrated in Figure 5–1. For the periodic slab configuration analyzed previously using the detailed modeling approach (see Figure 3–1), only two shell elements are needed in the reduced-order modeling approach, i.e., shell A for the thick portion of the slab and shell B for the thin portion (see Figure 5–1).

Figure 5–2 illustrates the layers of material used to represent the thick part of the slab (shell A) and the thin part of the slab (shell B) in the composite shell formulation. Based on the mesh sensitivity analysis in Chapter 3, in which the 4×4 coarse mesh was found to give reasonable results, four layers in the composite shell were used to represent the concrete in the upper portion of the concrete slab, and an additional four layers were used to represent the concrete in the rib (see Figure 5–2). An additional layer in shell A was used to represent the lower flanges of the steel decking, and an additional layer in shell B was used to represent the upper flange of the decking. Figure 5–2 illustrates the following two aspects of the reduced-order modeling approach, which are discussed in the subsequent subsections:

1. Reduction of the concrete density in the ribs to represent the tapered profile (Section 5.1.1)
2. Use of a “dummy material” to represent the voids between the ribs (Section 5.1.2)

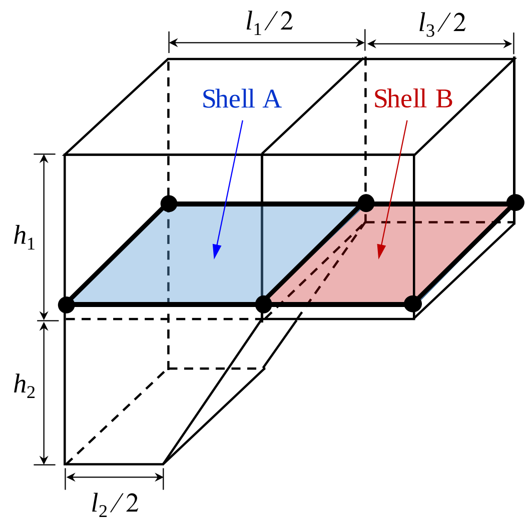

Figure 5–1. Representation of composite slab using alternating strips of shell elements

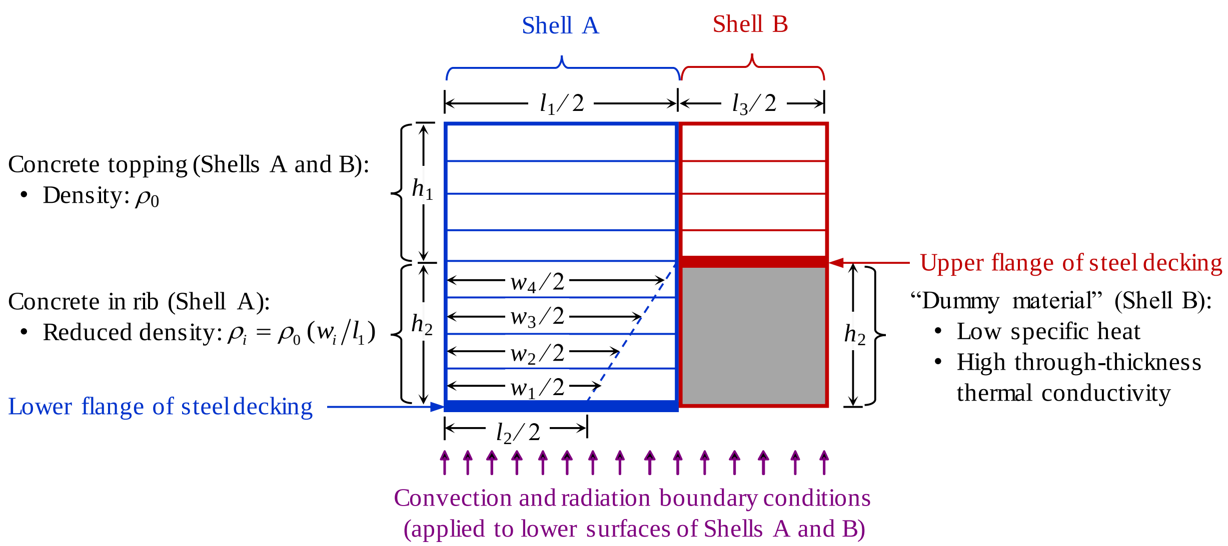

Figure 5–2. Layered-shell representation of thick and thin portions of composite slab

5.1.1 Reduction of Concrete Density in Ribs to Represent Tapered Profile

As observed previously in the parametric studies on the slab geometry in Section 4.4, the mass of concrete in the rib can significantly influence the temperatures in the slab above the rib. Therefore, accounting for the tapered profile of the rib is important in order to accurately represent the total mass of concrete in the rib, as well as its distribution. In the reduced-order modeling approach, the profile of the rib cannot be directly specified by using different widths for different layers, because the composite shell formulation assumes constant in-plane dimensions for all layers. Instead, the profile of the rib is accounted for in shell A by reducing the density of concrete in the rib to accurately represent the mass of concrete in each layer, As illustrated in Figure 5–2, the reduced concrete density for the *i*th layer of the rib, ρ_i, is calculated based on the ratio of the average rib width for that layer, w_i, to the total width at the top of the rib, l_1, as $\rho_i = \rho_0 \times (w_i / l_1)$, where ρ_0 is the concrete density.

5.1.2 "Dummy Material" to Represent Voids Between Ribs

In modeling the thin part of the slab (shell B), a "dummy material" with low specific heat and high through-thickness thermal conductivity is used to represent the voids between the ribs, with a height h_2 equal to the rib height, as illustrated in Figure 5–2. The key reason for incorporating the dummy material into shell B is to allow shell A and shell B to have the same thickness, which is required for proper modeling of in-plane heat conduction between corresponding layers of adjoining shell elements. Using the same thickness also allows the nodes of shell A and shell B to be defined in a common plane, which in this study was at mid-height of the thick portion of the slab (see Figure 5–1). In a coupled thermal-structural analysis, a structural material model with negligible stiffness and strength would also be assigned to the dummy material, as in Main and Sadek (2012), but this study considers thermal analysis only. Radiation and convection boundary conditions (Eq. (2.2)) are applied at the fictitious lower surface of shell B. A high through-thickness thermal conductivity for the dummy material, along with low specific heat (values of 100 W/(m·K) and 1 J/(kg·K), respectively, were used in this study), ensure an essentially equivalent temperature at the top of the dummy material, thus providing appropriate thermal boundary conditions for the upper flange of the steel decking. Radiation and convection boundary conditions are also applied to the bottom surface of shell A to model the heat input through the lower flange of the steel decking. Heat input through the web of the decking cannot be directly modeled in the layered composite shell formulation, because the web of the decking is not included in the model. However, the essentially uniform temperature through the depth of the dummy material (which is generally quite close to the gas temperature, as a result of the radiation and convection boundary conditions) does result in heat flux into the cooler adjoining layers in the rib of shell A, thus partially accounting for heat input through the web of the decking.

5.1.3 Comparison with Detailed Model Results for Baseline Slab Configuration

Figure 5–3 shows a comparison of temperature histories calculated from a reduced-order model of the baseline slab configuration (see Figure 3–12) with those calculated using the detailed modeling approach presented in Chapter 3. The same thermal boundary conditions (convection and radiation) were used in the reduced-order model as in the detailed model, with Eq. (3.1) used for the temperature-dependent emissivity of the galvanized decking and a constant value of 0.7 used for the emissivity of concrete at the unexposed surface. The results from the detailed model correspond to those presented previously in Figure 4–4 (dotted lines), except that layer-averaged temperatures are presented in Figure 5–3 rather than point estimates, for consistency with the shell-element temperatures obtained from the reduced-order model. Shell-element temperatures can be output at the lower, middle, and upper surfaces in LS-DYNA, and layer-averaged temperatures from the detailed model were calculated at consistent elevations, as illustrated in Figure 5–3. As noted in Section 5.1.2, the high through-thickness thermal conductivity of the dummy material ensures that the temperature at the fictitious lower surface of shell B is virtually equivalent to the temperature in the upper flange of the steel decking. For this reason, the upper flange of the steel decking is labeled as the lower surface in Figure 5–3b.

The temperature deviations between the reduced-order and detailed models in Figure 5–3 resulted from approximations inherent in the layered composite shell formulation, which underestimated the heat input through the web of the decking. This resulted in delayed heating just above the rib (middle surface in Figure 5–3a), where the reduced-order model underestimated the temperature by about 16 % at the end of the analysis. (The percent deviation at the end of the analysis is used to quantify discrepancies between the detailed and reduced-order models for the same reasons discussed in Section 3.2.1 in relation to comparisons with experimental data.) Better agreement was observed for the temperature histories at other locations.

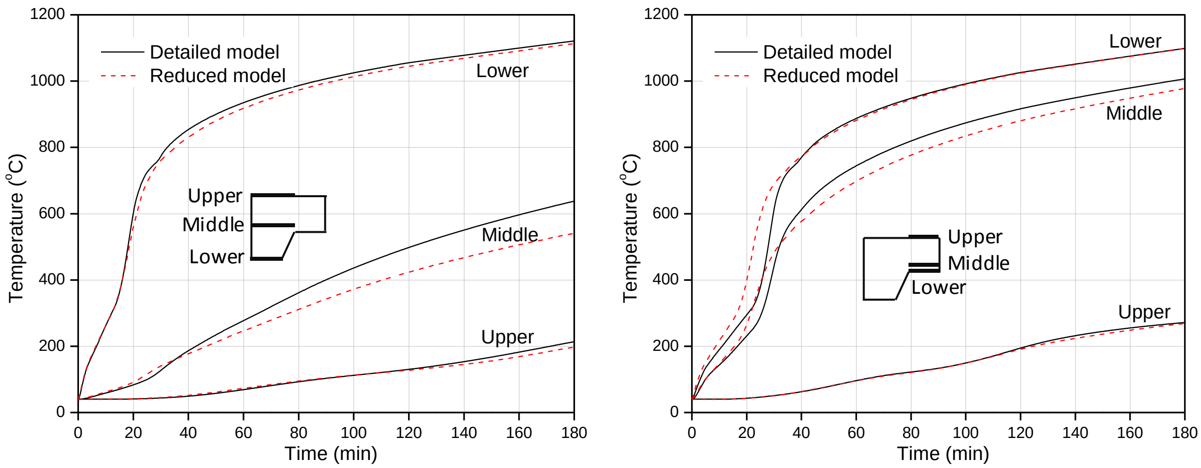

(a) (b)

Figure 5–3. Comparison of layer-averaged temperature histories from detailed model and reduced-order model: (a) thick portion of slab; (b) thin portion of slab

5.2 MODIFICATION OF SPECIFIC HEAT FOR CONCRETE IN THE RIBS

Several alternative methods were considered in an effort to better capture the heat input through the web of the decking. One option was to modify the thermal boundary conditions in order to provide additional heat input. However, the most effective approach was found to be through modification of the specific heat of the concrete in the rib. In this approach, an artificial specific heat, c'_p, was used for the concrete in the rib, while the actual specific heat, c_p, was used for the rest of the concrete in the slab. A reduction in the specific heat indirectly accounts for additional heat input through the web, since the reduced specific heat increases the thermal diffusivity, thus increasing the rate of heat flow through the rib. This approach allowed for improved accuracy in the temperature above the rib, with minimal effect on the temperatures at other locations in the slab, where the discrepancies in Figure 5–3 were already quite small.

The optimal value of c'_p/c_p was determined by minimizing the root-mean-square (RMS) deviation between the temperature histories from the reduced-order and detailed models, defined as follows:

$$T_{\mathrm{RMSD}} = \sqrt{\frac{\sum_{i=1}^{n}(T_{\mathrm{R}}(t_i)-T_{\mathrm{D}}(t_i))^2}{n}}\ , \tag{5.1}$$

where T_D and T_R are the temperatures obtained from the detailed and reduced-order models, respectively, t_i is the ith time sample, and n is the total number of time samples over the heating period. The RMS temperature deviation was evaluated for temperature histories from the middle surface of the thick part of the slab, where the largest discrepancy was observed in Figure 5–3.

First, the optimal value of c'_p/c_p was evaluated for the baseline slab configuration (Figure 3–12), as is discussed in Section 5.2.1. Then the influence of the slab geometry on the optimal value of c'_p/c_p was investigated, as is discussed in Section 5.2.2. Finally, Section 5.2.3 presents recommended values of c'_p/c_p to use for various slab dimensions.

5.2.1 Optimization of Specific Heat for Baseline Slab Configuration

Figure 5–4 shows a comparison of temperature histories from the detailed model and from reduced-order models with different ratios of specific heat for the concrete in the rib. Layer-averaged temperature histories from the middle surface of the thick portion of the slab are presented, and corresponding values of the RMS temperature deviation from Eq. (5.1) are presented in Figure 5–5. Figure 5–5 shows that a specific heat ratio of $c'_p/c_p = 0.7$ yielded the minimum RMS temperature deviation of $T_{RMSD} = 14$ °C, and inspection of Figure 5–4 confirms that this ratio produced the best agreement with the temperature history from the detailed model. Figure 5–6 shows a comparison of temperature histories from the detailed model with those from the reduced-order model for the optimal specific heat ratio of $c'_p/c_p = 0.7$ at all of the locations shown previously in Figure 5–3. Comparison of Figure 5–6 with Figure 5–3 shows considerably improved agreement at the middle surface of the thick portion of the slab, with no appreciable change in the discrepancies at other locations. For the optimal specific heat ratio of $c'_p/c_p = 0.7$ (Figure 5–6), the computed temperatures from the detailed and reduced-order models differed by 3 % or less at all locations.

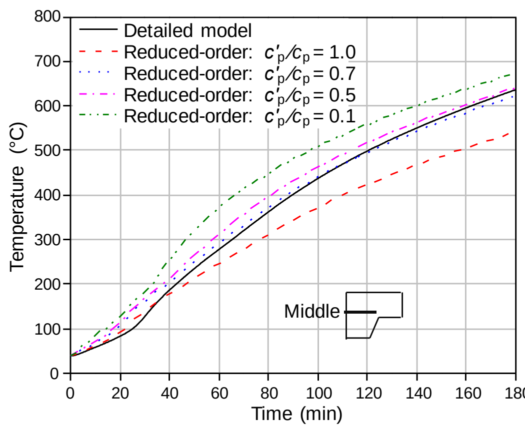

Figure 5–4. Layer-averaged temperature histories (middle surface of thick portion of slab) from detailed model and from reduced-order models with different specific heat ratios for concrete in the rib

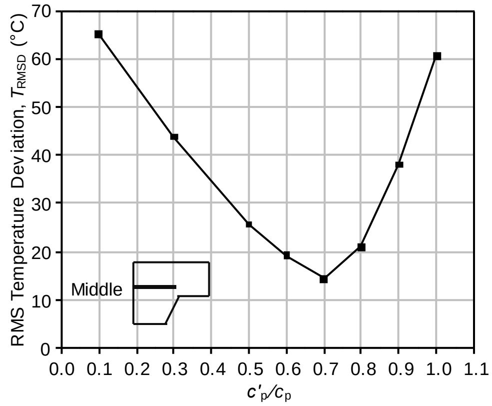

Figure 5–5. RMS deviation from detailed model of layer-averaged temperature histories (middle surface of thick portion of slab) from reduced-order models with different specific heat ratios for concrete in the rib

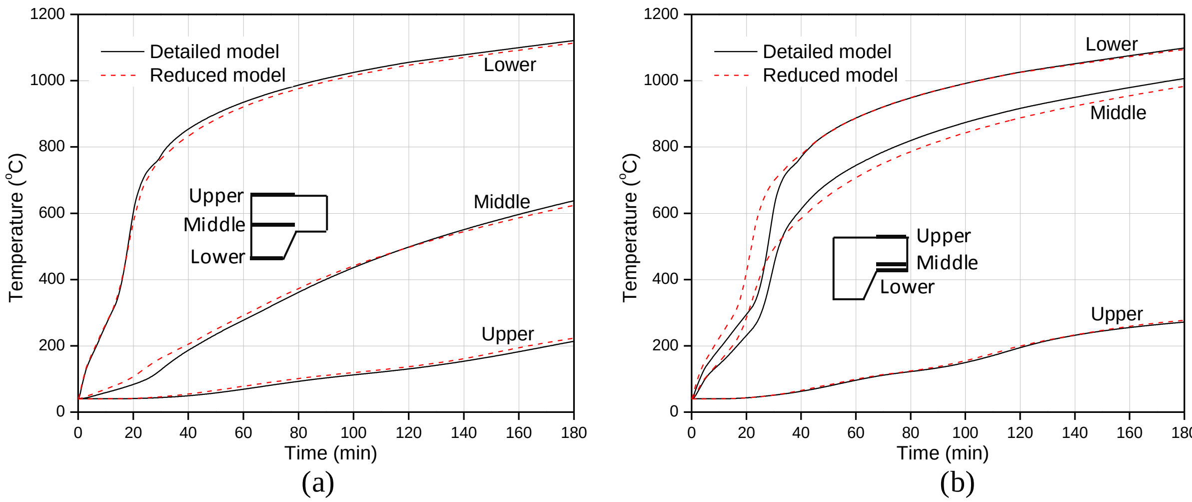

Figure 5–6. Layer-averaged temperature histories from detailed model and reduced-order model with optimal specific heat ratio of $c'_p/c_p = 0.7$: (a) thick portion of slab; (b) thin portion of slab

5.2.2 Influence of Slab Geometry on Optimal Value of Specific Heat

For the baseline slab geometry of Figure 3–12, artificially scaling the specific heat of concrete in the rib to $c'_p = 0.7c_p$ was found to minimize the RMS deviation between temperature histories from the detailed and reduced-order models. This section presents a parametric study on the influence of the slab geometry on the optimal ratio for the artificial specific heat, c'_p/c_p. Of particular interest in this study is the temperature history at the top of the rib (middle surface of the thick portion of the slab in Figure 5–3). The discrepancies between the detailed and reduced-order models were consistently largest at this location, as a result of heat input through the web of the decking, which cannot be directly modeled within the layered shell formulation. The geometric parameters that most strongly influence the temperature at the top of the rib were identified by reviewing the results of the parametric study previously presented in Section 4.4 on the influence of the five slab dimensions illustrated in Figure 3–12: h_1, h_2, l_1, l_2, and l_3. In that parametric study, which used the detailed modeling approach, the temperature at the top of the rib (point C) was found to be most sensitive to variations in the height of the rib, h_2 (see Figure 4–16), and the width at the top of the rib, l_1, which governs the angle of the web, α (see Figure 4–18). Variations in the other slab dimensions had a relatively minor influence on the temperature at the top of the rib. For this reason, a parametric study was conducted to investigate the influence of h_2 and l_1 on the optimal ratio of the artificial specific heat for concrete in the rib, c'_p/c_p. In this parametric study, h_2 and l_1 were varied independently, while the other slab dimensions were not varied from the baseline values (see Figure 3–12).

In addition to the baseline rib height of h_2 =75 mm, for which results were previously presented in Figure 5–4 and Figure 5–5, two additional rib heights of h_2 =50 mm and h_2 =100 mm were selected for the parametric study. For these two rib heights, Figure 5–7 shows a comparison of temperature histories from detailed models and from reduced-order models with different ratios of specific heat for the concrete in the rib. Layer-averaged temperature histories from the middle surface of the thick portion of the slab are presented in Figure 5–7, and corresponding values of the RMS temperature deviation (from Eq. (5.1)) are presented in Figure 5–8.

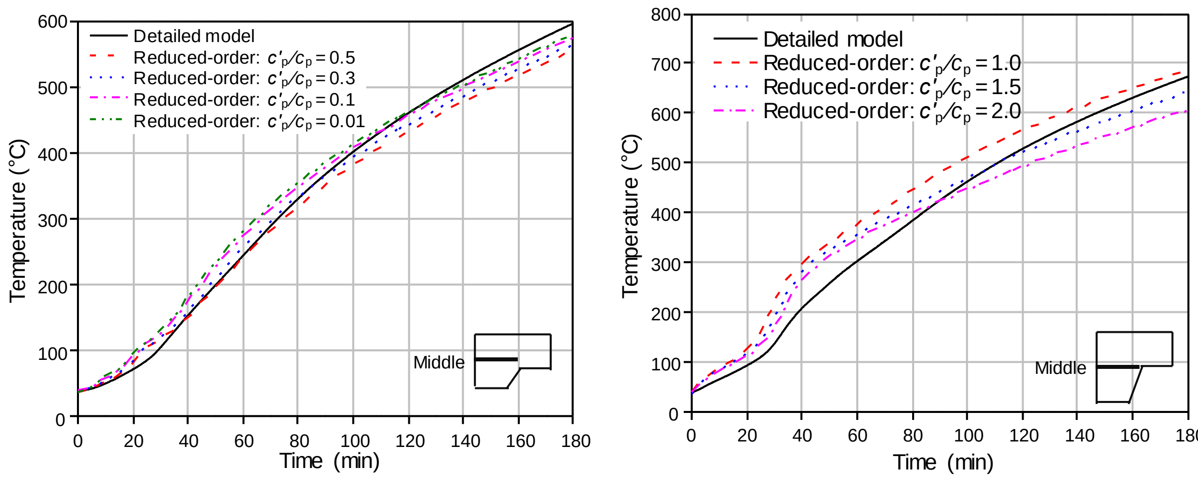

(a) (b)

Figure 5–7. Layer-averaged temperature histories (middle surface of thick portion of slab) from detailed model and from reduced-order models with different specific heat ratios for concrete in the rib: (a) h_2=50 mm; (b) h_2=100 mm

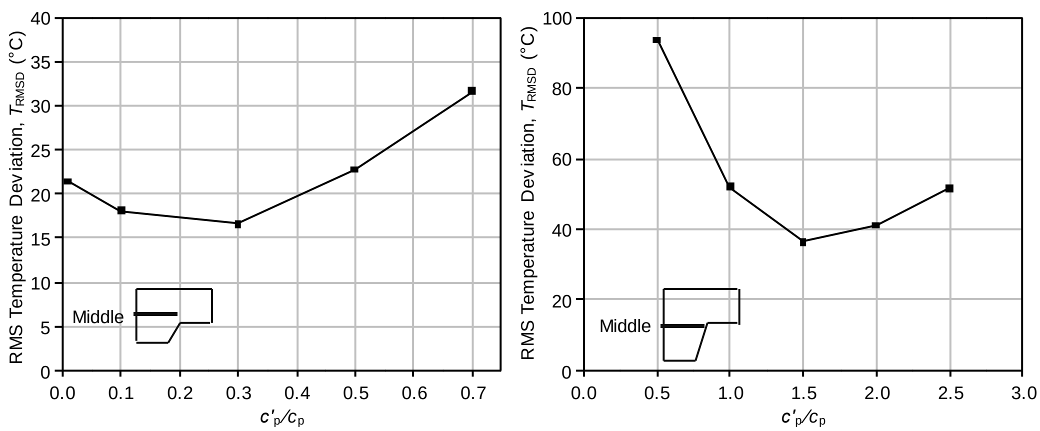

(a) (b)

Figure 5–8. RMS deviation from detailed model of layer-averaged temperature histories (middle surface of thick portion of slab) from reduced-order models with different specific heat ratios for concrete in the rib: (a) h_2=50 mm; (b) h_2=100 mm

For h_2 =50 mm, Figure 5–8(a) shows that a specific heat ratio of c'_p/c_p = 0.3 yielded the minimum RMS temperature deviation of T_{RMSD} = 16 °C. For h_2 =100 mm, Figure 5–8(b) shows that a specific heat ratio of c'_p/c_p = 1.5 yielded the minimum RMS temperature deviation of T_{RMSD} = 36 °C. For the baseline rib height of h_2 =75 mm, an optimal value of c'_p/c_p = 0.7 was previously identified from Figure 5–5. It is helpful to present these results in terms of the ratio of the concrete topping height to the rib height, h_1/h_2, where h_1 = 85 mm in all cases. Optimal specific heat ratios of c'_p/c_p = 0.3, 0.7, and 1.5 then correspond to height ratios of h_1/h_2 = 1.70, 1.13, and 0.85, respectively. These results indicate that when $h_1 > h_2$, the heat input through the web of the decking is underestimated. This corresponds to the case in which the dummy material spans less than half of the total slab height (see Figure 5–2). Artificially reducing the specific heat of concrete in the rib then helps to increase the flow of heat energy from the dummy material (in shell B) into the adjoining layers of the rib (in shell A), thus increasing the temperature at the top of the rib. Conversely, when $h_1 < h_2$, the heat input through the web of the decking is overestimated. This corresponds to the case in which the dummy material spans more than half of the total slab height. Artificially increasing the specific heat of concrete in the rib then helps to reduce the flow of heat energy from the dummy material into the adjoining layers of the rib, thus reducing the temperature at the top of the rib. The ratio h_1/h_2, which is inversely proportional to the height of the dummy material, is thus seen to be an important factor influencing the optimal ratio for the artificial specific heat of concrete in the rib.

In addition to the baseline value of l_1 =184 mm for the width at the top of the rib (web angle of α = 67°), two additional values of l_1 = 130 mm (α = 86°) and l_1 =250 mm (α = 50°) were selected for the parametric study. For these two values, Figure 5–9 shows a comparison of temperature histories from detailed models and from reduced-order models with different ratios of specific heat for the concrete in the rib. Corresponding values of the RMS temperature deviation for the temperature histories in Figure 5–9 are presented in Figure 5–10. Results for the baseline geometry were previously presented in Figure 5–4 and Figure 5–5. These results show that for l_1 = 130 mm, 184 mm, and 250 mm, minimum values of T_{RMSD} = 22 °C, 10 °C, and 14 °C were obtained for optimal specific heat ratios of c'_p/c_p = 0.5, 0.7, and 0.7, respectively. For l_1 =130 mm, it is noted that the RMS temperature deviation is almost equivalent for c'_p/c_p = 0.5 and for c'_p/c_p = 0.7, and thus a value c'_p/c_p = 0.7 is nearly optimal for all values of l_1. The optimal value of c'_p/c_p is thus seen to be much less sensitive to variations in l_1 than to variations in h_1/h_2. Recommended values of c'_p/c_p for varying slab geometry are presented in the following section.

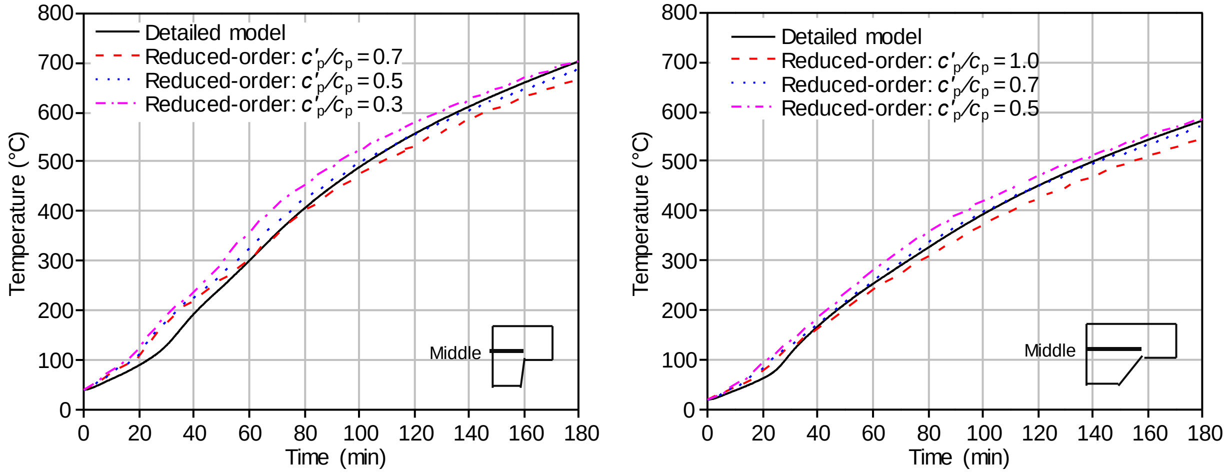

(a) (b)

Figure 5–9. Layer-averaged temperature histories (middle surface of thick portion of slab) from detailed model and from reduced-order models with different specific heat ratios for concrete in the rib: (a) l_1=130 mm; (b) l_1=250 mm

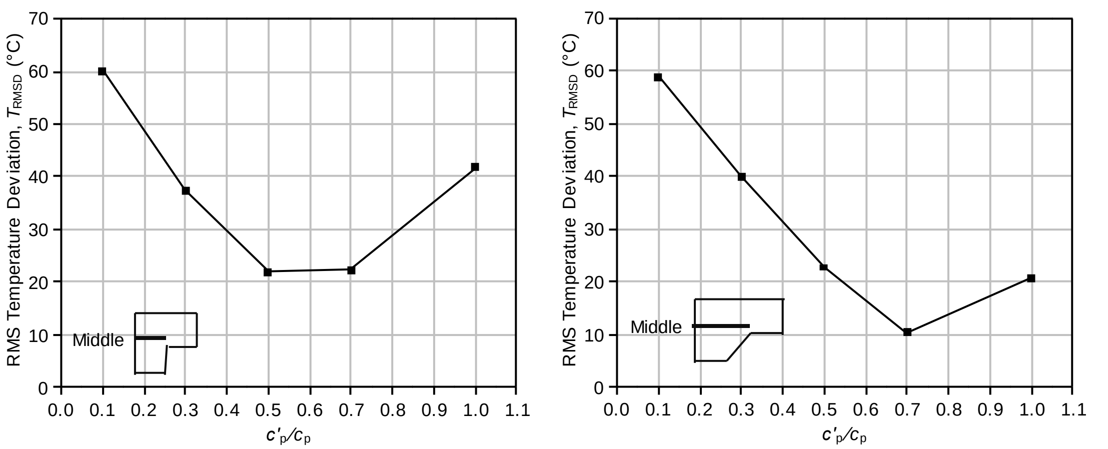

(a) (b)

Figure 5–10. RMS deviation from detailed model of layer-averaged temperature histories (middle surface of thick portion of slab) from reduced-order models with different specific heat ratios for concrete in the rib: (a) l_1=130 mm; (b) l_1=250 mm

5.2.3 Recommended Values of Specific Heat for Concrete in the Rib

The parametric study in the previous section demonstrated that modifying the specific heat of concrete in the rib could effectively reduce the discrepancies associated with heat input through the web of the decking, which can only be approximately modeled within the reduced-order, layered-shell approach. Heat transfer from the dummy material in shell B into the adjacent layers of the rib in shell A (see Figure 5–2) was significantly influenced by the specific heat in the rib, which allowed for improved accuracy through optimization of this value. Table 5–1 summarizes the results of this parametric study, presenting optimal values of the specific heat ratio c'_p/c_p and corresponding minimum values of the RMS temperature deviation for variations of the two slab dimensions, h_2 and l_1. The optimal value of the specific heat ratio was found to be insensitive to variations in l_1 but quite sensitive to variations in h_2, which is conveniently represented through the ratio h_1/h_2. For $h_1/h_2 > 1$, optimal values of the specific heat ratio c'_p/c_p were less than unity, while for $h_1/h_2 < 1$, the optimal value of c'_p/c_p was greater than unity.

Based on the results of the parametric study presented in Table 5–1, Figure 5–11 presents a practical recommendation for estimating the specific heat ratio c'_p/c_p as a function of h_1/h_2, in which c'_p/c_p is reduced linearly from a value of 1.0 for $h_1/h_2 = 1$ to a value of 0.5 for $h_1/h_2 = 1.2$. The slope of this linear reduction is based on the slope between the optimal values of c'_p/c_p for $h_2 = 75$ mm and $h_2 = 100$ mm (shown as solid circles in Figure 5–11). The recommended value of c'_p/c_p has an upper limit of 1.0 for $h_1/h_2 < 1$ because Figure 5–7b shows that values of c'_p/c_p exceeding 1.0 can result in underestimation of temperatures in the later stages of heating, which is not conservative, while Figure 5–8b shows that increasing c'_p/c_p beyond 1.0 produces only marginal reductions in the RMS temperature deviation. Artificially increasing the specific heat of concrete in the rib is thus not recommended. Similarly, the recommended value of c'_p/c_p has a lower limit of 0.5 for $h_1/h_2 > 1.2$, because Figure 5–8a shows that reducing c'_p/c_p below 0.5 produces only marginal reductions in the RMS temperature deviation.

Table 5–1. Optimal and recommended specific heat ratios for concrete in the rib for different slab dimensions

Slab Dimensions			Optimal Values		Recommended Values	
h_2 (mm)	l_1 (mm)	h_1/h_2	c'_p/c_p	T_{RMSD}	c'_p/c_p	T_{RMSD}
50	184	1.70	0.3	17 °C	0.5	23 °C
75	184	1.13	0.7	14 °C	0.67	25 °C
100	184	0.85	1.5	36 °C	1.0	52 °C
75	130	1.13	0.5	22 °C	0.67	22 °C
75	184	1.13	0.7	14 °C	0.67	25 °C
75	250	1.13	0.7	10 °C	0.67	23 °C

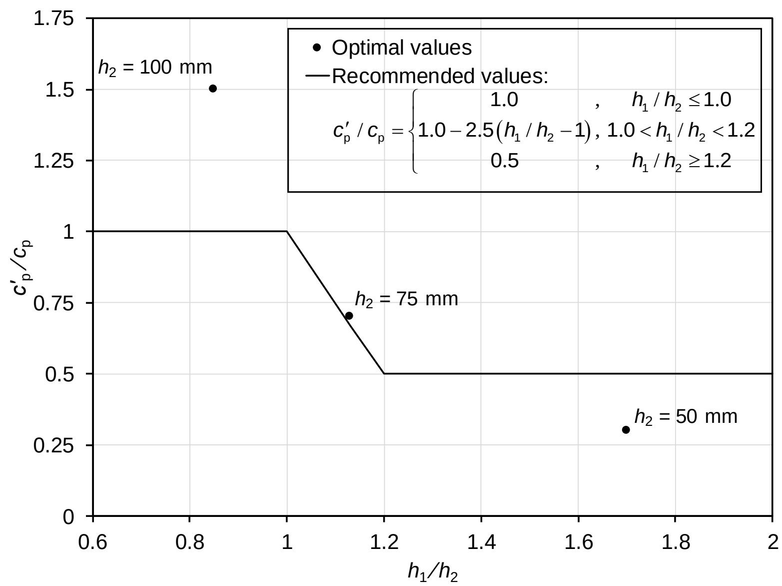

Figure 5–11. Recommended specific heat of concrete in the rib as a function of h_1/h_2

Figure 5–12 shows a comparison of temperature histories from detailed models and from reduced-order models using the recommended values of c'_p/c_p from Figure 5–11 for the three values of h_2 and the three values of l_1 considered in the parametric study of Section 5.2.2. The recommended values of c'_p/c_p used in these analyses are listed in Table 5–1 (column 6) along with the resulting RMS deviations between temperature histories from the detailed and reduced-order models in Figure 5–12. The RMS temperature deviations are slightly larger than those for the optimal value of c'_p/c_p, but in all cases the discrepancy between the detailed and reduced models at the end of the analysis was less than 10 %.

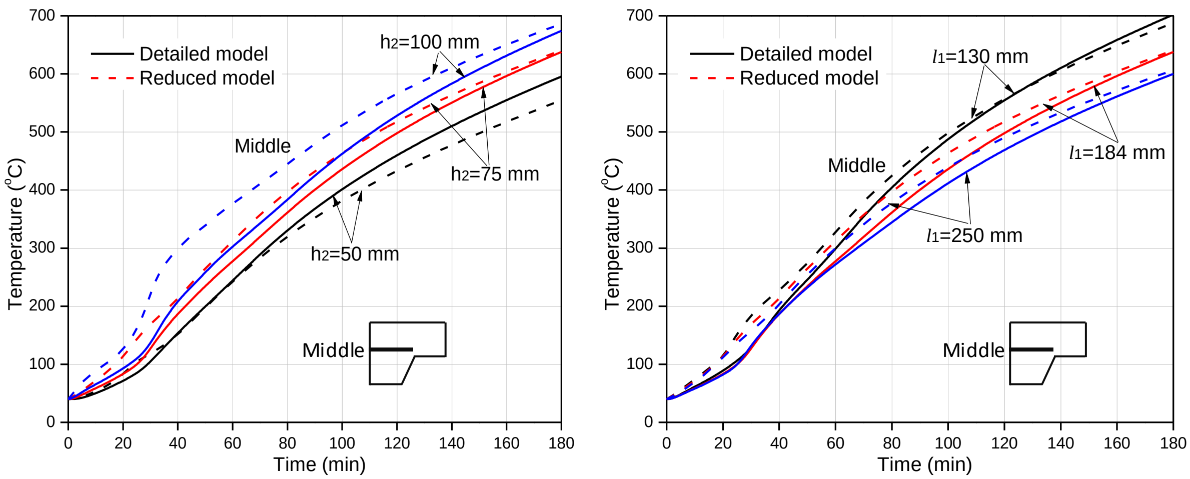

(a) (b)

Figure 5–12. Comparison of layer-averaged temperatures at the middle surface of the thick portion of the slab from detailed models and from reduced-order models with recommended values of specific heat in the rib: (a) for different values of h_2; (b) for different values of l_1

5.3 VALIDATION OF REDUCED-ORDER MODELING APPROACH

Chapter 3 presented validation of the detailed modeling approach against experimental results from the TNO test (Test 2 from Hamerlinck *et al.*, 1990) and the BRANZ test (Lim, 2003). The details for both tests were given in Section 3.2. This section describes the validation of the reduced-order modeling approach against the same two tests. In the reduced-order models, modification of the specific heat for concrete in the rib was based on the recommendation in Figure 5–11.

Figure 5–13 presents a comparison of the measured temperature histories from the TNO slab test with the computed temperatures from the detailed and reduced-order models. For consistency with the experimental measurements, point temperatures rather than layer-averaged temperatures are presented from the numerical models (i.e., nodal temperatures, rather than element temperatures, are presented from the reduced-order model). The TNO slab had a height ratio of $h_1/h_2 = 0.96$, for which Figure 5–11 recommends a specific heat ratio of $c'_p/c_p = 1.0$, and therefore, no modification of the specific heat of concrete in the rib was used in the reduced-order model of the TNO test. For comparison with the computed results, the measured temperature at point M (mid-height of the thick portion of the slab) was obtained by interpolation of measured temperatures at adjacent points (points A and G in Figure 3–2). Note that the proposed emissivity of galvanized steel defined in Eq. (3.1) was used in both the detailed and reduced-order models, which gave improved agreement relative to the model of Hamerlinck et el. (1990) at most locations (see Section 3.2.1), but somewhat overestimated the measured temperature at Point K.

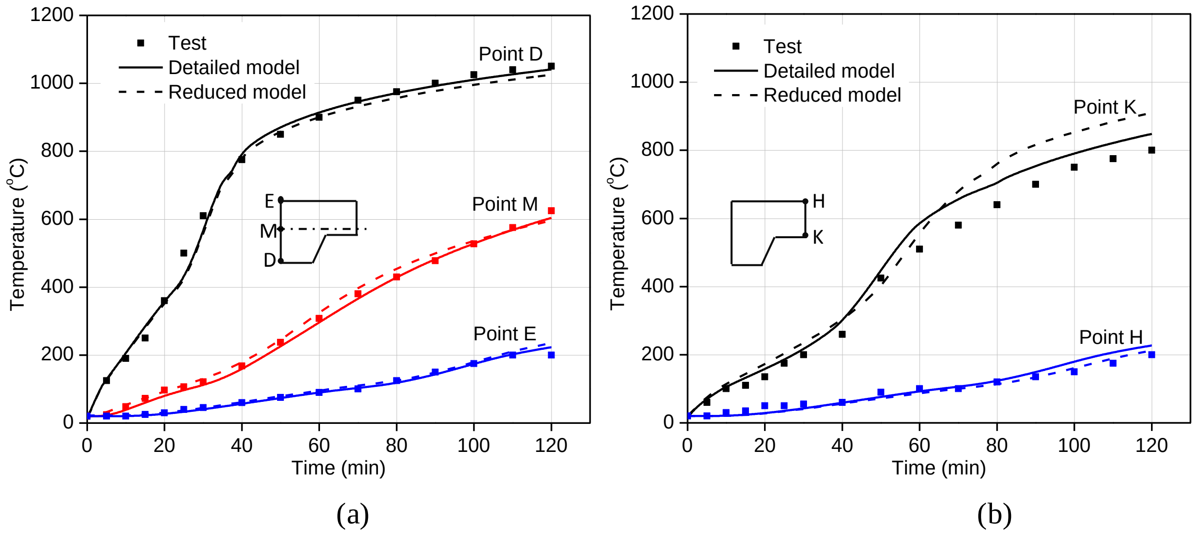

Figure 5–13. Comparison of measured temperatures from TNO test (Hamerlinck et al. 1990) with computed temperatures from detailed and reduced-order models: (a) thick portion of slab; (b) thin portion of slab

Table 5–2 presents RMS deviations between the measured and computed temperature histories shown in Figure 5–13 (calculated from Eq. (5.1)), as well as percent deviations at the end of the test. The largest discrepancies were at point K, where the RMS temperature deviations were 42 °C and 73 °C for the detailed and reduced-order models, respectively. At all other locations, the RMS temperature deviations were less than 30 °C. The largest percent deviations at the end of the test were +14 % and +17 % for the detailed and reduced-order models, at points H and E, respectively.

Table 5–2. Root-mean-square and percent deviations between measured and computed temperatures at the five locations shown in Figure 5–13 for the TNO test (Hamerlinck et al., 1990)

	RMS Temperature Deviation, T_{RMSD}		Percent Deviation* at End of Test	
Location	Detailed Model	Reduced-Order Model	Detailed Model	Reduced-Order Model
Point D	25 °C	30 °C	−1 %	−2 %
Point M	11 °C	14 °C	−3 %	−5 %
Point E	7 °C	10 °C	+11 %	+17 %
Point K	42 °C	73 °C	+6 %	+14 %
Point H	17 °C	12 °C	+14 %	+6 %

* Positive deviations indicate that the model was conservative.

Figure 5–14 shows a comparison of the measured temperature histories from the BRANZ slab test (Lim, 2003) with the computed temperatures from the detailed and reduced-order models. The BRANZ slab had a height ratio of $h_1/h_2 = 1.4$, for which Figure 5–11 recommends a specific heat ratio of $c'_p/c_p = 0.5$, and therefore, the specific heat of concrete in the rib was reduced to half of the value used elsewhere in the slab.

The computed temperatures at point A (for both the detailed and reduced-order models) were higher than the measured results as a consequence of the debonding of the steel decking from the concrete that occurred during the test, as discussed previously in Section 3.2.2. Table 5–3 presents RMS deviations between the measured and computed temperature histories shown in Figure 5–14 (calculated from Eq. (5.1)), as well as percent deviations at the end of the test. Because of the debonding that occurred, the largest discrepancies were at point A, where both the detailed and reduced-order models had RMS temperature deviations of approximately 140 °C and percent deviations of approximately +10 % at the end of the test. Better agreement was observed at point M, where the RMS temperature deviations were 32 °C or less and the percent deviations at the end of the test were −6 % or less for both the detailed and reduced-order models.

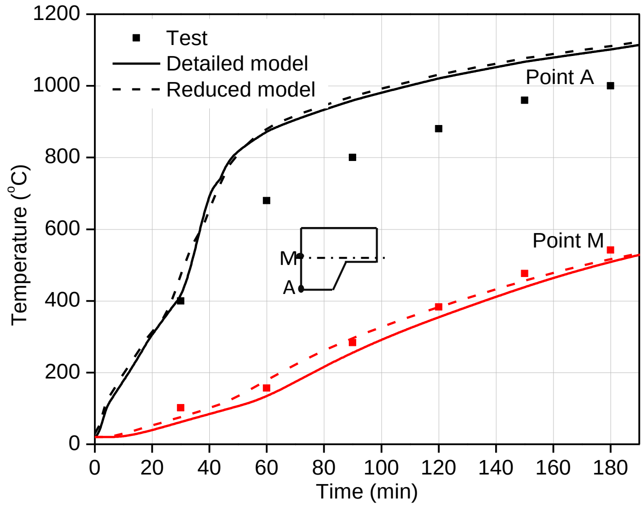

Figure 5–14. Comparison of measured temperatures from BRANZ test (Lim, 2003) with computed temperatures from the detailed and reduced-order models

Table 5–3. Root-mean-square and percent deviations between measured and computed temperatures at the two locations shown in **Figure** 5–14 for the BRANZ test (Lim, 2003)

	RMS Temperature Deviation, T_{RMSD}		Percent Deviation* at End of Test	
Location	Detailed Model	Reduced-Order Model	Detailed Model	Reduced-Order Model
Point A	131 °C	142 °C	+10 %	+11 %
Point M	32 °C	20 °C	−6 %	−5 %

* Positive deviations indicate that the model was conservative.

5.4 SUMMARY

This chapter presented the development of a reduced-order modeling approach for heat transfer in composite slabs, using layered shell elements. The performance of the reduced-order model was validated against experimental results and was also verified against the detailed models. A summary of key findings is provided below:

- The proposed reduced-order modeling approach used a layered composite shell formulation. The geometry of composite slabs can be captured using alternating strips of shell elements to represent the thick and thin portions of the slab.
- Modifying the specific heat of the concrete in the ribs was found to be an effective method of accounting for heat input through the web, which was the greatest challenge in modeling the thermal behavior of composite slabs by using shell elements. Optimized values of specific heat were recommended for slabs with different geometries.
- A linear reduction in the density of concrete with depth in the rib can be used to account for the tapered profile of the ribs.
- The voids between the ribs were represented and filled by a "dummy material" with low specific heat and high through-thickness thermal conductivity. This made the thick and thin portions of the slab had the same thickness, which enabled the in-plane heat conduction between adjoining shell elements to indirectly consider the heat input from the web and also facilitate the development of structural models.

Chapter 6
SUMMARY AND CONCLUSIONS

This report presented detailed and reduced-order finite-element modeling approaches for heat transfer in composite floor slabs with profiled steel decking. The detailed modeling approach used solid elements for the concrete slab and shell elements for the steel decking. The reduced-order modeling approach used layered shell elements for both the concrete slab and the steel decking. The detailed models were validated against standard fire test results, and then used to conduct a parametric study. The influence of the thermal boundary conditions, thermal properties of the materials, and slab geometry on the temperature distribution in the composite slabs was studied. For the reduced-order modeling approach, alternating strips of layered shell elements were used to represent the slab. Elements representing the thick portion of the slab used a gradient in the density of concrete to represent the profile of the ribs. Elements representing the thin portion of the slab incorporated a layer of dummy material with the same height as the ribs, to represent the voids between the ribs. The specific heat of the concrete in the rib was also modified to more closely approximate the heat input through the web of the decking, which cannot be directly modeled in the layered-shell approach. Optimization of the modified specific heat was performed for a range of slab geometries, and an equation for the recommended modification factor was proposed as a function of the ratio between the height of the concrete topping and the height of the rib.

Based on the study reported herein, the following conclusions were reached.

- The heat transfer in composite slabs can be analyzed using a detailed model composed of solid elements for the concrete slab and shell elements for the steel decking. The heat transfer analysis of composite slabs was not particularly sensitive to the mesh size, and a mesh of 4 elements over the height of the rib, 4 elements over the height of the upper portion of the slab, and 4 elements for one half-width of the rib was sufficient to yield reasonable accuracy for the temperature distribution in the slab.
- The temperature distribution in composite slabs was highly non-uniform due to the presence of ribs. Heat input through the upper flange of decking governed the temperature distribution in the thin portion of the slab. The temperature distribution in the rib was governed by the heat input through the lower flange and the web of decking. The web and the upper flange had a significant influence on the temperature in the upper flat region above the rib. Therefore, the heat input through the web must be properly accounted for. This was a key challenge in the development of the reduced-order modeling approach using layered shell elements, in which only the heat input through the lower and upper flanges can be directly modeled.
- The thermal conductivity of concrete had a larger influence on the unexposed surface of the slab than the fire-exposed surface. The ASCE models of concrete conductivity are quite similar to the upper limit in EC4, which is recommended for the numerical analysis. The specific heat had less influence on the temperature than did the conductivity, and a constant value of 1000 J/(kg·K) can be used for simple analytical calculations. The moisture content of concrete had a significant influence on the temperature distribution. An increase of 1 % in moisture content led to an enhancement of the fire resistance by about 5 minutes which is caused by the retardation of the concrete temperature rise at 100 °C and above.

- The height of the rib, h_2, had a significant influence on the temperature in the rib but less influence on the temperatures on the unexposed surface and in the thin portion of the slab. The height of the upper continuous portion of the slab, h_1 (i.e., the thickness of the concrete topping), was the most significant factor affecting the temperatures at the unexposed surface, and thus the fire resistance of composite slabs. The fire resistance of composite slabs, based on the thermal insulation criterion at the unexposed surface, was typically governed by the maximum temperature at the unexposed surface, rather than the average temperature of the unexposed surface.
- For the reduced-order model of composite slabs using layered shell elements, the heat input through the web of the decking can be reasonably accounted for by incorporating a dummy material in the thin portion of the slab, in conjunction with modifying the specific heat of concrete in the rib. The recommended modification factor for the specific heat in the rib, c'_p/c_p, can be taken as 0.5 for slabs with $h_1/h_2 > 1.2$ and as 1.0 for slabs with $h_1/h_2 < 1.0$, with a linear interpolation between these values for h_1/h_2 between 1.0 and 1.2.
- The reduced-order modeling approach can be used to model heat transfer in composite slabs, provided that the heat input from the web of the steel decking is properly accounted for as proposed herein. Comparison of measured temperature histories with those computed from the reduced-order model showed that the largest root-mean-square temperature deviation (excluding a location where debonding is known to have influence the temperature measurement) was 73 °C, with a maximum deviation of 17 % for the temperature at any location at the end of the test.

References

ACI 216.1-14 (2014). Code Requirements for Determining Fire Resistance of Concrete and Masonry Construction Assemblies. ACI/TMS Committee 216, Michigan, USA.

Alashker Y., El-Tawil S., and Sadek F. (2010). Progressive collapse resistance of steel-concrete composite floors. J. Struct. Eng., 136(10), 1187-1196.

ASCE (1992). Structural Fire Protection. ASCE Manual and Reports on Engineering Practice No. 78. ASCE Committee on Fire Protection, New York.

Bailey C.G., White D.S. and Moore D.B. (2000). The tensile membrane action of unrestrained composite slabs simulated under fire conditions. Engineering Structures, 22: 1583-1595.

Bednar J., Wald F., Vodicka J. and Kohoutkova A. (2013). Experiments on membrane action of composite floors with steel fibre reinforced concrete slab exposed to fire. Fire Safety Journal, 59: 111-121.

Both C. (1998). The fire resistance of composite steel-concrete slabs. Ph.D. dissertation, Delft University of Technology, Delft, Netherlands.

Both K., Stark J.W.B. and Twilt L. (1992). Thermal shielding near intermediate support of continuous span composite slabs. Proceedings of 11th International Specialty Conference on Cold-formed Steel Structures, USA, 309-321.

EN 1994-1-2. (2005). Eurocode 4 Design of composite steel and concrete structures: Part 1.2: General rules, Structural fire design, European Committee for Standardization (CEN), Brussels.

EN 1991-1-2. (2009). Eurocode 1 Actions on structures: Part 1.2: General actions, Actions on structures exposed to fire, European Committee for Standardization (CEN), Brussels.

Elghazouli A.Y. and Izzuddin B.A. (2000). Response of idealised composite beam-slab systems under fire conditions. Journal of Constructional Steel Research, 56: 199-224.

Elghazouli A.Y., Izzuddin B.A., and Richardson A.J. (2000). Numerical modelling of the structural fire behaviour of composite buildings. Fire Safety Journal, 35: 279-297.

Foster S., Chladna´ M., Hsieh C., Burgess I., Plank R. (2007). Thermal and structural behaviour of a full-scale composite building subject to a severe compartment fire. Fire Safety Journal, 42:183-199.

Gillie M., Usmani A.S. and Rotter J.M. (2001). Modelling of heated composite floor slabs with reference to the Cardington experiments. Fire Safety Journal, 36:745-767.

Guo S. and Bailey C.G. (2011). Experimental behaviour of composite slabs during the heating and cooling fire stages. Engineering Structures, 33:563-571

Guo S. (2012). Experimental and numerical study on restrained composite slab during heating and cooling. Journal of Constructional Steel Research, 69: 95-105.

Hamerlinck R., Twilt L. and Stark J. (1990). A numerical model for fire-exposed composite steel/concrete slabs. Proceedings of tenth International Specialty Conference on Cold-formed Steel Structures, USA, 115-130.

Huang Z., Burgess I.W. and Plank R.J. (2000). Effective stiffness modelling of composite concrete slabs in fire. Engineering Structures, 22(9): 1133-1144.

International Organization for Standardization (ISO). 2014. *Fire-resistance tests – Elements of building construction, ISO 834-11*, Geneva, Switzerland.

Izzuddin B.A., Tao X.Y. and Elghazouli A.Y. (2004). Realistic modelling of composite and R/C floor slabs under extreme loading-Part I: Analytical method. Journal of Structural Engineering, 130(12): 1972-1984.

Kirby B.R. (1997). British steel technical European fire test programme design, construction and results. Fire, static and dynamic tests of building structures. London.

Kolsek J., Saje M., Planinc I. and Hozjan T. (2014). A fully generalised approach to modelling fire response of steel-RC composite structures. International Journal of Non-Linear Mechanics, 67: 382-393.

Kodur V. (2014). Properties of concrete at elevated temperatures. ISRN Civil Engineering, 1-15.

Kwasniewski L. (2010). Nonlinear dynamic simulations of progressive collapse for a multistory building. Engineering Structures, 30, 1308-1318.

Lamont S., Usmani A.S. and Gillie M. (2004). Behaviour of a small composite steel frame structure in a “long-cool” and a “short-hot” fire. Fire Safety Journal, 39:327-357.

Li G.Q. and Wang P.J. (2013). Advanced analysis and design for fire safety of steel structures. Zhejiang University Press, Hangzhou and Springer-Verlag Berlin Heidelberg.

Lienhard J.H. A Heat Transfer Textbook. Phlogiston Press, Cambridge, MA, 2011

Lim L.C.S. (2003). Membrane action in fire exposed concrete floor systems. PhD Dissertation. University of Canterbury, Christchurch, New Zealand.

Lim L.C.S., Buchanan A., Moss P. and Franssen J.M. (2004). Numerical modelling of two-way reinforced concrete slabs in fire. Engineering Structures, 26:1081-91.

Livermore Software Technology Corporation (LSTC). (2014). LS-DYNA Keyword User’s Manual, R7.1, LSTC, Livermore, California.

Phan L.T., McAllister T.P., Gross J.L. and Hurley M.J. (2010). Best practice guidelines for structural fire resistance design of concrete and steel buildings. Technical Note 1681, NIST, USA.

Main J.A. and Sadek F. (2012). Robustness of steel gravity frame systems with single-plate shear connections. Technical Note 1749, NIST, USA.

Main J.A. (2014). “Composite floor systems under column loss: Collapse resistance and tie force requirements.” *J. Struct. Eng.*, 140(8), A4014003.

Nag P.K. (2008). *Heat and Mass Transfer*. Tata McGraw-Hill Publishing, New Delhi.

Pantousa D. and Mistakidis E. (2013). Advanced modelling of composite slabs with thin-walled steel sheeting submitted to fire. Fire Technology, 49: 293-327.

Sadek F., El-Tawil S., and Lew H.S. (2008). “Robustness of composite floor systems with shear connections: Modeling, simulation, and evaluation.” *J. Struct. Eng.*, 134(11), 1717-1725.

Sanad A.M., Lamont S., Usmani A.S. and Rotter J.M. (2000). Structural behaviour in a fire compartment under different heating regimes—part 1 (slab thermal gradients). Fire Safety Journal, 35: 99-116.

Sanad A.M., Lamont S., Usmani A.S. and Rotter J.M. (2000). Structural behaviour in a fire compartment under different heating regimes—part 2 (slab mean temperatures). Fire Safety Journal, 35: 117-130.

Wellman E.I., Varma A.H., Fike R. and Kodur V. (2011). Experimental evaluation of thin composite floor assemblies under fire loading. Journal of Structural Engineering, 137(9): 1002-1016.

Yu X.M., Huang Z., Burgess I.W. and Plank R.J. (2008). Nonlinear analysis of orthotropic composite slabs in fire. Engineering Structures, 30(1): 67-80.

Zhao B., Roosefid M., Breunese A. et al. (2011). Connections of steel and composite structures under natural fire conditions (COSSFIRE). Technical Report ECSC.